UNIVERSITA' DEGLI STUDI DI PADOVA

Dipartimento di Ingegneria Industriale DII

UNIVERSITÀ
DEGLI STUDI
DI PADOVA

Corso di Laurea Magistrale in Ingegneria Aerospaziale

A Multi-objective shape optimization of an S-Duct intake through NSGA-II genetic algorithm

Academic Supervisors:
Prof. Ernesto Benini
Prof. Mark Savill

Authors
Aurora Rigobello 1081845

5 Dicembre 2016

A.A. 2015/2016

When everything seems to be going against you, remember that the airplane takes off against the wind, not with it.

Henry Ford

Abstract

A Multi-Objective shape Optimization analysis was applied to a civil S-duct intake, for reducing total pressure losses and flow distortions.

The parameterization of the geometry was set up with Free Form Deformation method and it was enhanced with respect to a previous investigation. Duct deformation depends on 36 variables.
NSGA-II genetic algorithm was implemented in the optimization loop to manage the design vector and improved duct performances.
More than 600 geometries were tested within 3D CFD simulations; duct efficiency was defined through two functions that have been improved during the optimization: Pressure Recovery and Swirl angle.

The analysis gave an enhancement of 19% for pressure recovery coefficient and a reduction of 13% for swirl distortion.
New geometry configurations were investigated and the results were compared to those of a prior project.

Acknowledgements

I would like to express my sincerely gratitude to my supervisors Prof. Ernesto Benini and Prof Mark SAVILL, for giving me the opportunity to work on this topic and strengthen the collaboration between Padova and Cranfied Universities.

I would also like to thanks my Research Fellow, Dr. Nicola CHIEREGHIN, for his constant help during these months; his advices and supports were essential for completing the thesis.

A sincere “Thank you” to my parents Flavia and Luca, my brother and sister. Their presence and support were fundamentals to complete this “journey”, especially in these last months. After all, family is always there.

I would also like to thank all my friends and those who were really there for me.

Contents

List of Figures

List of Tables

Abbreviations

AIP	Aerodynamic Interface Plane
CFD	Computational fluid Dynamics
BLI	Boundary Layer Ingestion
BWB	Blended Wing Body
DNS	Direct Numerical Solution
DP	Distributed Propulsion
EA	Evolutionary Algorithm
FFD	Free form Deformation
FMG	Full Multi Grid
GA	Genetic Algorithm
IGV	Inlet Guide Vane
LES	Large Eddy Simulation
MOOP	Multi Objective Optimization Problem
NSGA	Non-dominated Sorting Genetic Algorithm
PR	Pressure Recovery
RANSE	Reynolds Averaged Navier Stokes Equation
RMSE	Root Mean Squared Error
SBX	Simulated Binary cross(X)over
SF	Scale Factor
UAV	Unmanned Aerial Vehicle

Symbols

A_1	S-duct inlet area	m^2
A_2	S-duct outlet area	m^2
$B_{i,j,k}$	B-spline Blending function	-
C_p	Specific heat at constant pressure	kJ kg^{-1} K^{-1}
c_p	Total pressure coefficient	-
d_1	S-duct inlet diameter	m
d_2	S-duct outlet diameter	m
M	Mach number	-
$\dot{m}$	Mass flow	kg s^{-1}
P_t	Total pressure	Pa
p	Static pressure	Pa
PR	Pressure recovery	-
$P_{i,j,k}$	FFD initial control point location	-
$q_{i,j,k}$	FFD deformed control point location	-
R	S-duct curvature radius	m
T	Temperature	K
t	Time	s
u	Velocity component in x direction	m s^{-1}
v	Velocity component in y direction	m s^{-1}
V_θ	Velocity component in tangential direction	m s^{-1}
w	Velocity component in z direction	m s^{-1}

α	Swirl angle	rad
θ	Tangential angle	rad
ρ	Density	kg m^{-3}
ϕ	S-duct cross section polar angle	rad

Chapter 1

Introduction

Aircraft gas turbine engine is mainly composed by an intake, a gas generator and a nozzle; it generates a high enthalpy flow that is accelerated, producing the necessary thrust for flying an entire airplane. A proper functioning of each of these elements is crucial for the propulsion.
This project focuses on the first component mentioned, the intake, and the improvements achievable by changing its shape.
The intake is a duct designed to convey air to the compressor, with low flow distortions and a suitable Mach number for stable operations; it decelerates the stream and increases its static pressure. Unfortunately, this pressure recovery implies an adverse gradient along the duct that leads to flow separation on walls, causing losses and non-uniformities.

1.1 Context and Background

S-duct intakes are a particular type of inlet for modern aircraft propulsion systems. They present the typical cross section growth for subsonic diffusers, associated with a curved centerline; mainly due to the double bend, these channels are affected, not only by a wide region of flow separation, but also by secondary streams (vortices). Wellborn's studies (1) show how those irregularities compromise engine performances and flow uniformity at the compressor Aerodynamic Interface Plane (AIP).
Despite these disadvantages, S-duct represents a flourishing topic for experimental and computational researches and it is used in modern aircraft gas turbine engines.

Briefly considering military applications, this kind of intake has been adopted in advanced missiles and combat aircrafts, because it suits the design features of this sector. The current trend is to reduce mass, size, fuel consumption and observability, increasing reactivity and engine operations range, hence shortened S-intakes perfectly satisfy these goals. As the engine is integrated within the airframe under the fuselage, weight and length reductions are expected, hence the airplane is more compact and the costs are reduced as well.

Figure 1.1 *Example of UAVs: Salty Dog 501 X47-B.*

Furthermore, this configuration leads to shield the compressor from a direct observation of radar waves and to preserve the whole structure. Tangible examples of successful applications of S-duct are the Unmanned Aerial Vehicles (UAVs), such as Salty Dog (Fig.1.1), the military General Dynamics Falcon F-16 (Fig.1.2) and McDonnell-Douglas F-18.

Figure 1.2 *Example of General Dynamics Falcon F-16.*

Regarding civil applications, there are several commercial aircrafts that made use of highly convoluted intakes, such as the Lockheed Tristar L-1011 and the Boeing

727. They combine three engines, one of them is placed at a different height in the rear part of the plane; its S-duct inlet is situated within the tail (Fig.1.3).

Figure 1.3 *Example of Lockheed Tristar L-1011.*

Nowadays S-duct inlets studies are mostly connected with the promising Distributed Propulsion (DP), an advanced concept of propulsion systems, to which this thesis and the previous ones carried on at Cranfield are closely related.

1.2 Distributed Propulsion for Civil Application

The main topics for civil aircraft design refer to energy consumption and the environment; through the Subsonic Fixed Wing project (2), NASA recognized four technology aims that have to be improved for achieving higher performances. These goals concern the reduction of emissions, noise and fuel consumption and the improvement of flight range (3). For these reasons, the American agency has studied a new propulsion vehicles concept: Distributed Propulsion (Fig.1.4) that was concretely developed only in the 1990s.

Until the Fifties, great part of the airplanes have been conceived using the classical configuration: two or four engines placed under the wings or on the fuselage, to reduce aerodynamics interactions with vehicle functioning. Distributed Propulsion indeed, expects to couple the airframe and the propulsion system, using several smaller and compact propellers integrated in the wings, so that the plane fully benefits from this innovative design. In a more specific definition from (2): “ DP in aircraft application is the spanwise distribution of the

propulsive thrust stream such as … the efficiencies are mutually maximized to enhance the vehicle mission".

Figure 1.4 *A practical application of Distributed Propulsion.*

The main improvements obtained through this design are: the reduction of noise, nacelle viscous drag, flow separation and weight, the perfecting of engine fuel efficiency and the easily replacement of small engines. Those are the reasons why this new type of installation perfectly fits the SFW NASA goals and represents the future in aeronautical propulsion.

Furthermore, recent researches conducted by Boing (4) are focusing on the achievable advantages of Boundary Layer Ingestion (BLI) in planes that combine Blended Winged Body (BWB) and DP.

Figure 1.5 *Experimental model of Boing BWB-450.*

BLI implies that an aft placed engine ingests part of the low momentum boundary layer of the fuselage, in order to reduce fuel consumption; in this configuration, the propellers are no more set on pylons but they are embedded in the airframe,

almost removing nacelle losses (5) and (6). BWB considers the aircraft as a single body where “the fuselage is also a wing, an inlet for the engines and a pitch control surface” (4), gained substantial benefits in terms of aerodynamic efficiency, emissions, noise and payload. An example is the experimental model Boing BWB-450, shown in Fig.1.5.

1.3 Objectives and Expectations

As mentioned, DP technology requires S-duct intakes, but their shapes cause pressure and velocity distortions distributions, negatively affecting compressor operations. Thus, recently experimental and computational projects have emerged to accurately predict intake aerodynamics, trying to make the flow as uniform as possible. Cranfield University is focusing on this topic through PhD and MSc students’ researches that were particularly important for the development of this thesis (7), (8), and (9).

The primary aim of the project is to reduce flow distortions and losses within the S-duct through a shape optimization process. This is a multi-objective analysis based on the Non-Dominated Sorting Genetic Algorithm (NSGA-II), which tries to minimize two functions at the same time: total pressure losses and swirl angle at the duct outlet.
Following a previous investigation on S-ducts (7), the baseline geometry parameterization was enhanced, doubling the variable vector size and increasing project fidelity level; later it was tested and validated with literature results. Then two optimization simulations were run with different ranges variation of variable vector, bringing solver convergence and maximum shape deformation to the limit. Consequently, new geometries were analyzed and compared with the results of a former study.

This work is expected to provide a better comprehension of the flowfield within the S-shaped inlet; not always a high fidelity analysis contributed to improve the results, but surely they will be more in line with the physical phenomenon, properly describing flow losses and distortions.

This project aims to be a contribution for future developments, together with those of the last year, extending the knowledge about shape design for an appropriate engine operation in DP propulsion systems and providing a range of useful data for practical applications.

1.4 CFD and MOOP

Physical observations and experimental tests are not always possible and usually expensive. Computational Fluid Dynamics (CFD) is a software largely used by engineers and researchers to adequately simulate and predict flow behavior, solving Navier-Stokes equations. CFD helps to analyze the three-dimensional stream within the S-ducts. In the current work, ANSYS (10) license of Cranfield University was used on ASTRAL cluster that allows parallel processing. (11)

The mathematical side of the simulation consists in a Multi-Objective Optimization Problem (MOOP). MOOP tries to enhance two or more objective functions, changing the design parameters and finding trade-off solutions. A genetic algorithm was chosen and implemented in the analysis.
The entire analysis were automated in a loop process, written in and controlled by Python scripts, described in Appendix B.

Chapter 2

Literature Review

First of all, this section explains the main characteristics of a subsonic flow in an S-duct intake. Secondly, it introduces a general overview of theoretical and experimental researches that have been fundamental in the resolution and design of this project. Most relevant and useful parameters will be underlined during this presentation.

2.1 S-duct Flowfield Physics

S-duct is affected by different types of non-uniformities, mainly caused by its bended shape: total pressure, swirl angle and total temperature distortions. The latter will not be considered in this thesis analysis, because it does not concern civil application.
The word distortion includes both spatial changes that magnitude changes. There are several type of swirl, but the one that principally affects an S-duct is composed by two counter rotating vortex, clearly visible at AIP.
Total pressure distortions are related to boundary layer separation, which occurs after the second bend, generating a wide low-momentum region. Moreover, it should be considered the classical pressure losses due to the cross-section growth of subsonic diffuser.

Pressure recovery and swirl angle are the parameters chosen for describing flow characterization, described in the following sections.

2.1.1 Swirl

In a cylindrical flow, the velocity vector could be divided into its tangential and axial components, respectively V_θ and V_z, or in its radial and circumferential components; the latter is also known as swirl and it causes the whirling motion of the stream.
The first goal function is the swirl angle, defined as:

$$\propto = arctan(V_\theta / V_z) \tag{2.1}$$

It is considered positive if it has the same rotation direction of the compressor.
As Fig.2.1 shows, the swirl physically represents the angular deviation between the local velocity vector and the normal vector, both referred to the AIP plane.

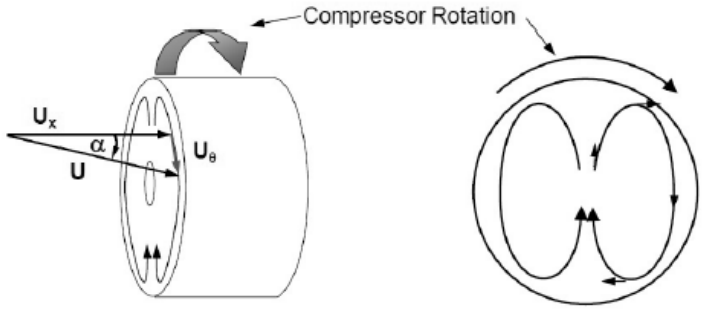

Figure 2.1 *Velocity components in determining the Swirl (12).*

In aeronautics, there are four different types of swirl that could affect a flow within an S-pipe and these are briefly described below: *paired*, *bulk*, *cross-flow* and *tightly-wound* swirl.

Tightly-Wound vortex: It is also known as inlet-ground vortex for its characteristic of attaching to airplane surfaces or to the ground. This type of swirl is highly energetic, compact: it is generated by several mechanisms such as tip vortices, leading-edge extensions and near-static operations in ground proximity, as shown in Fig.2.2 and Fig.2.3.

Figure 2.2 *Tightly-Wound vortex attached to the ground (12).*

Figure 2.3 *Tightly-Wound vortex attached to airplane surfaces (12).*

***Cross-flow swirl*:** This kind of swirl is conceptually identical to the paired one, except for the presence of a uniform velocity in cross-flow direction. Usually, it can be observed in lift fans or in turboshaft and turboprop with bifurcated intake ducts.

Bulk swirl: The bulk swirl occurs when the entire flowfield spins in one direction about the compressor axis; if flow rotates in the same direction of the engine it is called co-rotating swirl, otherwise it is named counter-rotating swirl.
This distortion is defined as “the circumferential mean value of the flow angle for each constant radius *R*” (12).
Bulk swirl can be generated internally or externally to the duct, but the former circumstance is more important for the project; it occurs when the “inlet flow experienced a non-axisymmetric total-pressure gradient, normal to angle plane,

which combines with static-pressure gradient of the S-bend flow" (7). Fig.2.4 displays how the sideslip flow separation at the inlet causes a wide low-energy region that starts to rotate. Its intensity mainly depends on geometric parameters and flow conditions.

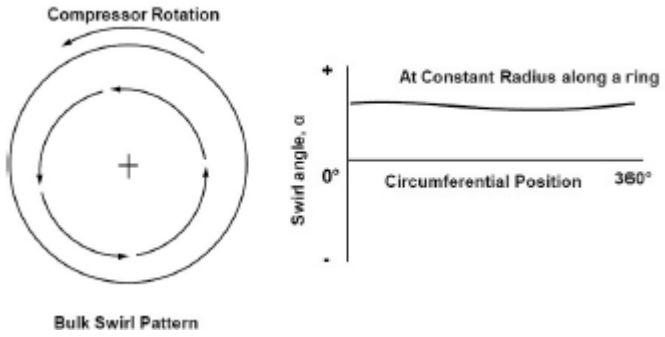

Figure 2.4 *Bulk swirl distortion (12).*

Paired Swirl: This is the most common and relevant type of swirl that takes place in a bent duct. If the vortexes have the same magnitude, the swirl is *called twin swirl*, otherwise simply *offset paired swirl*. There are two different explanations for this phenomenon, one based on pressure gradient and the other one based on vorticity.

Basically, the latter is due to the fact that flow vorticity vector is turned by the duct shape, inducing flow rotation along a third direction.

Fig.2.5 shows the second justification in detail. Firstly, considering an ideal situation, a flow in a bent duct experiences an increasing static pressure related to the increasing radius of turn, in order to balance centrifugal forces, and a conforming reduction of flow velocity. Since the flow is non ideal, boundary layers must be taken in account: velocity distribution varies from zero at the walls to its maximum in flow core; the flowfield is subjected to a non-uniform momentum distribution. The high velocity core is deflected towards the outside part of the bend, while the low-momentum fluid near the walls, which cannot cross an adverse pressure gradient region, slips around the walls towards the inside part of the bend. The combination of the high and low velocity streams causes two paired of counter-rotating vortexes.

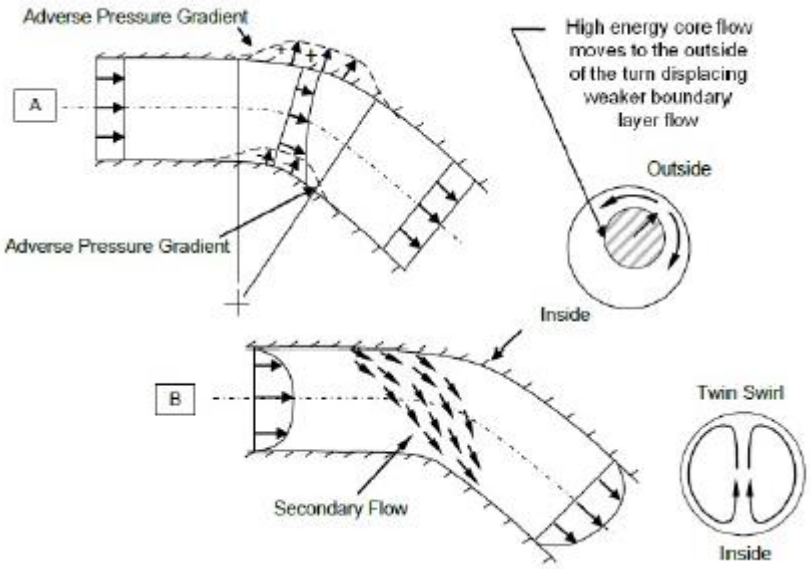

Figure 2.5 *Paired swirl formation based on pressure gradient theory.*

2.1.2 Total pressure losses

As mentioned, the duct presents different separate regions: a small one on the walls caused by the cross-section growth, and the other one generates by duct bends; the wider are these regions, the greater are total pressure losses. Moreover, the latter region blocks a large part of the duct, increasing flow velocity, shear stresses and producing additional losses (see Fig.2.6). Also vortices are a source of pressure losses, in fact they convey the low-energy region towards the center, reducing both magnitude and uniformity pressure distribution.
Reducing these losses is the second goal function of the thesis; for this purpose, it was chosen the Pressure Recovery (PR) coefficient at the AIP:

$$PR = P_{t,out}/P_{t,in} \tag{2.2}$$

PR is the ratio between inlet and outlet total pressure values. Obviously, it provides just an area-averaged evaluation and it does not indicate exactly where these events are located, but this coefficient suits for a general comprehension of flow behavior.
For minimizing the losses, the right coefficient used is C_p, simply defined as:

$$C_p = 1 - PR \tag{2.3}$$

2.1.3 Flow separation

Flow separation is a common aerodynamics phenomenon that occurs in diffusing channel; it is due to the boundary layer detachment off the walls, because the flow experiences an adverse pressure gradient in increasing cross-section area. This separation causes a reverse flow and vortices formation, as visible in Fig.2.6.

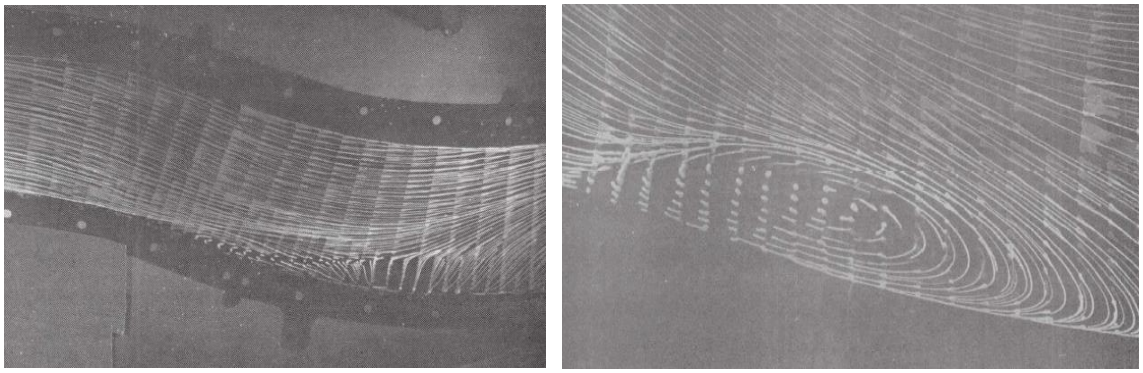

Figure 2.6 *Flow separation within an S-duct (1).*

In diffusing S-intake, flow detachment is placed right after the first bend and it occupies a wide downstream region, as proved by Wellborn's experiments (1). It is generated, not only by the growing area, but also by the curved centerline.

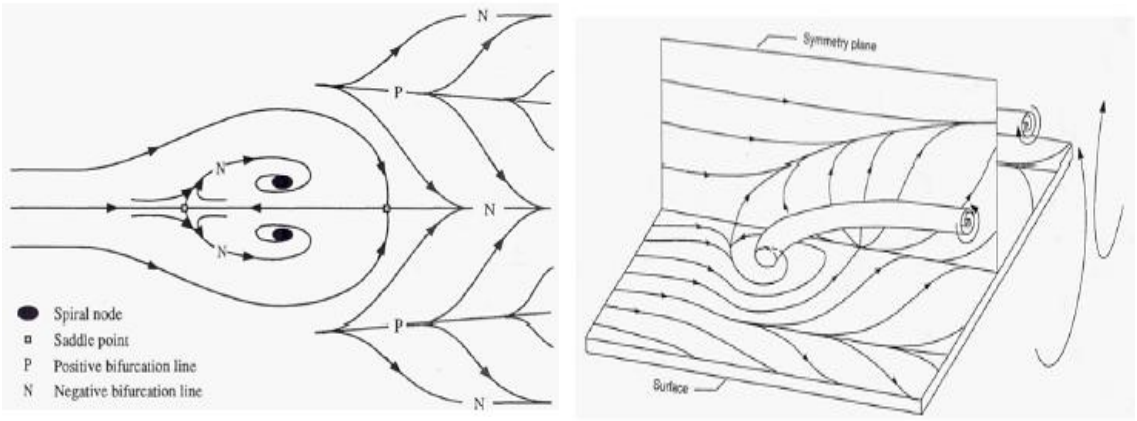

Figure 2.7 *3-D separation surfaces in an S-duct (1).*

Fig.2.7 displays separation region in S-ducts; clearly it is a 3D complex singularity, described with stream-surfaces. From literature, the flow presents two symmetrical negative bifurcations from an upstream saddle point, converging into a spiral node. Then, positive bifurcations surround other two negative ones.

This symmetrical configuration is highly instable, but it perfectly represents flow lines behavior.

2.2 Prior Observations on S-duct

As mentioned in Chapter 1, S-duct intake represents a flourishing topic both for military and civil applications; in the last decades, several researches have been performed to better understand flowfield characterization in order to reduce flow distortions and improve duct performances.
The first projects were based on experimental researches; recently, the progresses in computational analysis allow to simulate the flow with mathematical models, facilitating S-duct studies.

2.2.1 Experimental Researches

In 1943, Weske (13) conduced the first experiment on duct with elbows; the project analyzed velocity distributions and pressure drops in elliptical and circular cross-section shapes. The tests were performed at different flow velocities, between 100 and 300 ft/s, proving how the most important parameters that influence pressure drops are the curved centerline and the ratio between inlet and outlet radius.
In 1972 for the first time, Bandson's project (14) showed the presence of the two counter-rotating vortexes at AIP plane, responsible of the low total pressure section. He also analyzed several parameters (static and total pressure, shear stresses…) and their variations in the separate region. Moreover, Anderson (15) demonstrated how these vortices are inviscid, hence they depend on a non-uniform inlet velocity profile, as mentioned in swirl theory.

The most relevant experimental research was performed by Wellborn (1) in 1993; he tested compressible flows within an S-ducts at NASA Lewis Research Centre, providing several data, about aerodynamic parameters and flow separation mechanism, that were useful for the following CFD projects. The duct shape will be presented later in Chapter 4, as it is the starting point for the current thesis.

The experiment facility is shown in Fig.2.8. Firstly, it involves a *Settling Chamber* for conditioning and making the flow more uniform, thanks to screens and meshes; then, the flow is accelerated in the *Contraction Nozzle* and stabilized within a short straight passage. Finally, it enters the S-duct, *Test Section*, where it is analyzed; later it is conveyed towards the *Exhaust Region*.

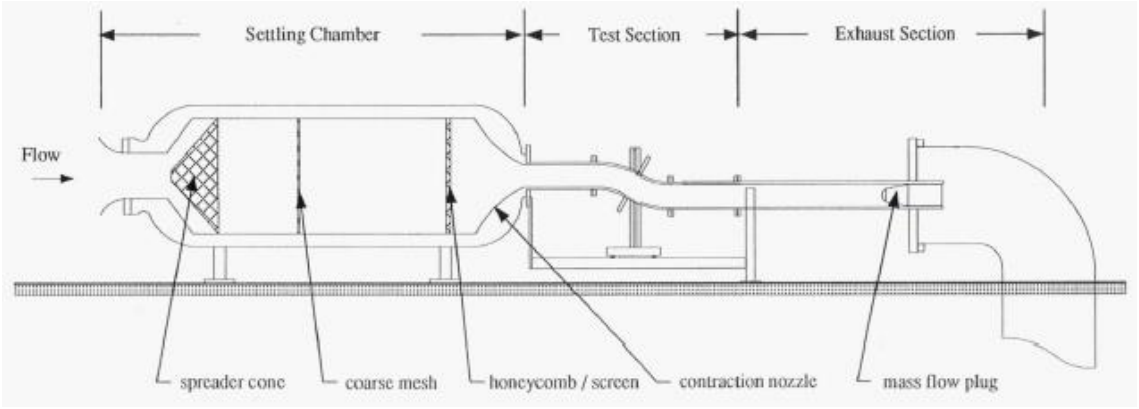

Figure 2.8 *Facility Scheme of Wellborn (1).*

All flow measurements were conducted on five planes perpendicular to the center line, with a total of 220 static pressure taps, located at constant angle of 10°, 90°, and 170°; the stream presented a constant Mach number equal to 0.6 and a Reynolds number of 2.6 $x10^6$.

The experiment showed flowfield complexity; in correspondence of the first bend, a large separate region takes place, evolving in a vortex on the symmetry plane and in two counter-rotating vortices at the AIP plane. These secondary flows cause the huge total pressure drop. Moreover, Wellborn underlined that the flow is still symmetric and how the boundary layer is extremely separate from duct walls.

Fig.2.9 displays static pressure trend along the duct for three circumferential positions. Pressure drop is clearly visible near section C.

Instead, Fig.2.10 shows total pressure contours distribution in the five reference planes. It is visible the boundary layer detachment towards duct core; low-momentum region starts in plane C and it evolves like in plane E, occupying great part of the cross-section.

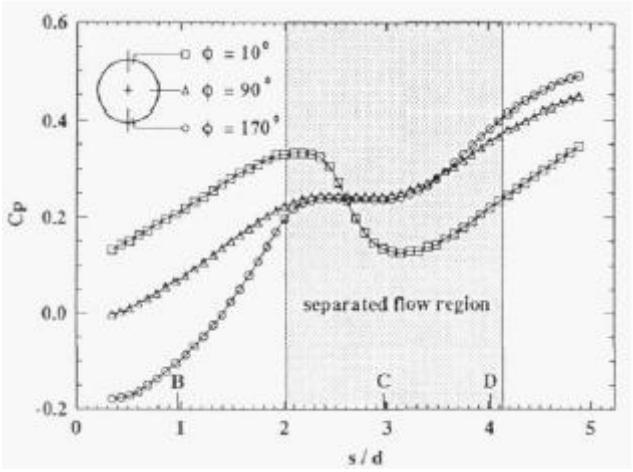

Figure 2.9 *Static pressure trends for three position (1).*

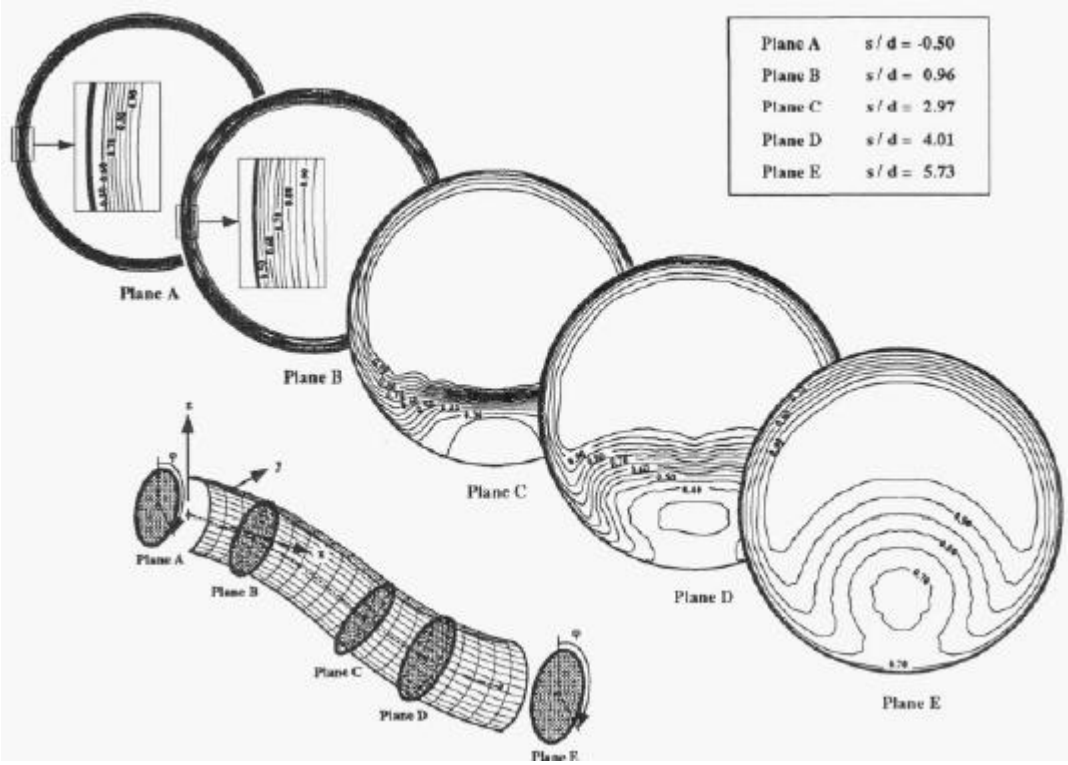

Figure 2.10 *Total pressure contours on the five planes (1).*

The two vortices continually convey low momentum fluid towards the center, decreasing both pressure and velocity magnitude that their distributions.

2.2.2 Computational Researches

Nowadays, CFD tools are relevant for the design phase; they have been improved throughout the years and now they are able to accurately predict flow behavior and validate experimental data. Several projects were useful in defining the best mesh, turbulence model and CFD settings for a proper flow simulation.
Smith's work [] was precious in analyzing the difference between O-grid and H-grid and how well these grids predict distortions intensity and location. He suggested to use a hybrid mesh, with the O-grid near the wall and the H-grid in the center.
For steady phenomena, Delot's (16) project is one of the most recent and important studies about S-duct (2006). She based her experimental work on Wellborn's geometry, scaling it up, visible in Fig.2.11.

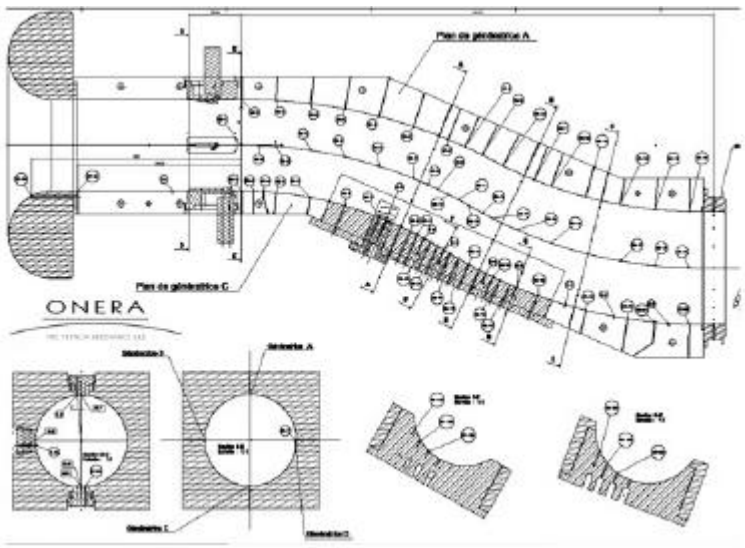

Figure 2.11 *Facility Scheme of Delot's experiment (16).*

Moreover, she carried out several computational tests for defining the best set up that best reproduce real flow. She compared several meshes, solver codes and turbolence models; the project stated that Fluent solver best matches the separate region and well predicts low pressure region, even though it presents some discrepancies in PR coefficient, which is too high with respect to the real one. Unfortunately, it is impossible to accurately predict pressure recovery and flow distortions at the same time.

Fiola's research (17) tested the geometry with Fluent solver and four types of turbulence, concluding that the *k-w* SST model best suits PR prediction along the centerline; since this project concern with minimizing pressure losses, *k-w* SST turbulence model was chosen.
Other several researches were carried out in the last years for a better comprehension of flow psychics and for improving its performances, such as the insertion of vortex generator devices and unsteady simulations (18).

2.2.3 Optimizations

Recently, optimization processes were applied to S-duct intake for enhancing its characteristics; in particular, two projects performed at Cranfield were fundamental for this thesis.
These simulations modifying duct shape, perturbing control points positions; this concept will be presented later in Chapter 4.

Rectangular Cross-Section: Furlan's study (19) investigated the flow within a rectangular cross-section. The optimization aim was to minimize the parameters: $C_{p,loss}$ and DC_{60}.
The first is an area-averaged total pressure coefficient, while the second is a distortion factor for flow distortions at the outlet.
The results are displayed in the Fig.2.12: the optimized geometry presents a bottom bump that allows distortions reductions. It reduced the coefficients respectively of 58% and 54%.

Figure 2.12 *Furlan's results: baseline (left), optimized (right) (19).*

Circular Cross-section: this study was performed by Guglielmi (7) and it is the starting point of this and other two thesis (8), (9). It will be described later, as it is used for comparing the results of the current project.

Briefly, it used two objective functions: 1-PR and α; it analyzed in detail three types of geometries: best pressure recovery, best swirl angle and a trade-off solution. Fig.2.13 and Fig.2.14 show Pressure Recovery distributions and swirl distribution in the optimized configurations, with respect to the baseline. The improvements achieved are clearly visible.

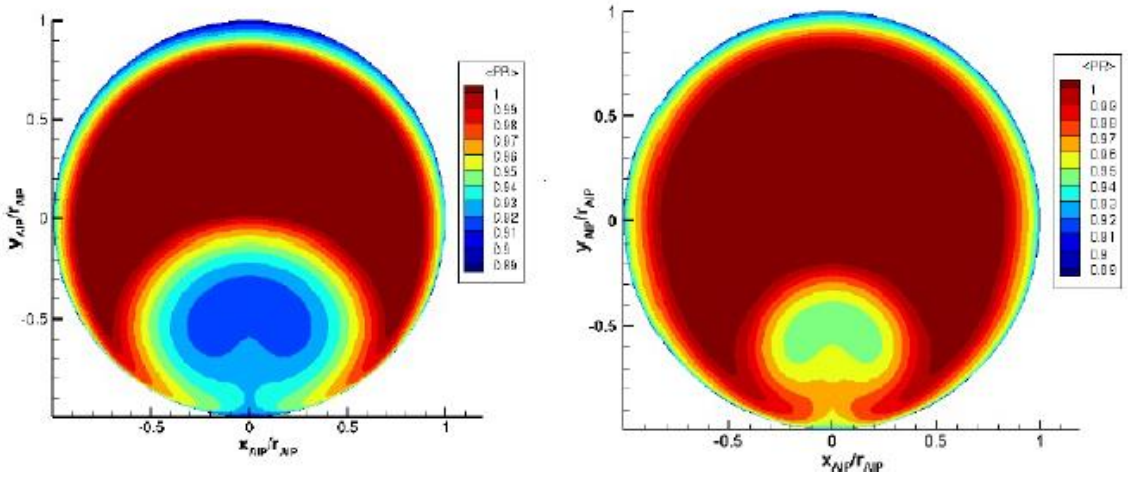

Figure 2.13 *PR distributions: baseline (left) and best PR (right) geometries (7).*

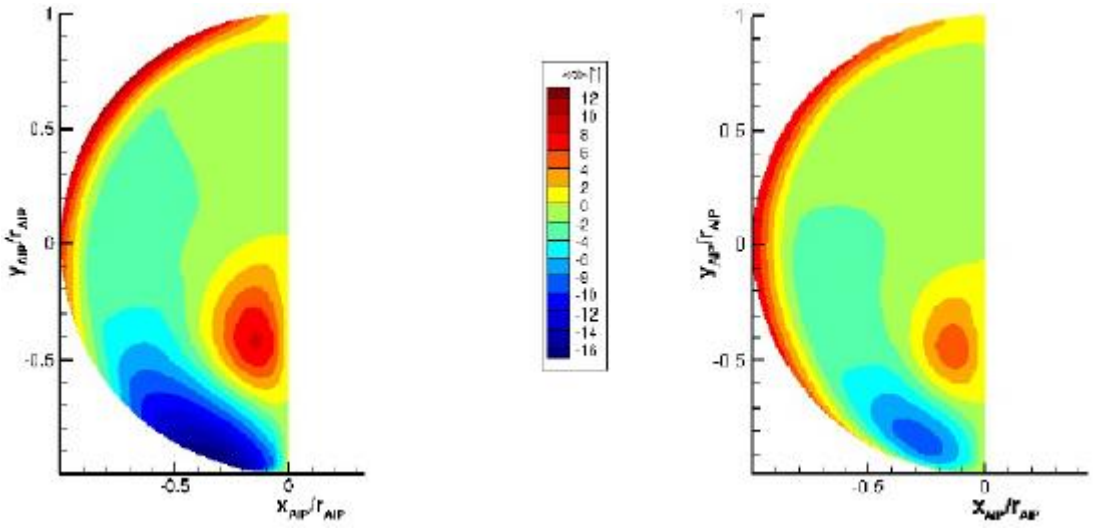

Figure 2.14 *Swirl distributions: baseline (left) and best PR (right) geometries (7).*

Other two important projects were performed at Cranfield. The first one (9) is about a multi-objective optimization with surrogate models, trained on Guglielmi's data; it investigated about surrogate prediction capability in S-duct application. The second one (8) is about an unsteady analysis of the first project results with different meshes; in particular, it stated how a medium mesh gives results that are similar to a fine mesh ones, and that there are no great differences between the half and the entire duct.

Following these encouraging results, this project deals with an improved multi-objective optimization, doubling the decision variables for increasing flow physics knowledge and exploring new geometry configurations.

Chapter 3

Multi-Objective Optimization

This Chapter briefly describes the main features and peculiarities of an Optimization process. Most of the real problems, from Engineering to Economy and Logistic, rarely concern a single objective function because of Nature's complexity: there are multiplex conflicting targets preventing univocally define which the best solution is. Hence, the role of the Designer is to make a reasonable choice, considering projects requirements. In the Aeronautical field these decisions might regard the efficiency of an engine, the losses or consumption of an airplane or the structural strength of the fuselage.

3.1 The Problem and its Loop

In Mathematics, an Optimization problem consists in finding the optimal set(s) of decision variables that minimizes or maximizes a goal function, given a defined domain and its relative constrains. Actually each optimization problem could be mutated into a minimization problem, due to the fact that the maximum of a function $f(x)$ is merely the minimum of the function $-f(x)$.
A Multi-Objective Optimization Problem (MOOP) is generally described by the relations below:

$$\text{Find} \quad \bar{x} = x_1, \dots, x_n \tag{3.1}$$

$$\text{that minimize} \quad f_j(\bar{x}) \quad \forall j = 1, \dots, J \tag{3.2}$$

$$\text{subject to:} \quad g_l \geq 0 \quad \forall l = 1, \dots, L \tag{3.3}$$

$$h_k = 0 \quad \forall h = 1, \dots, K \tag{3.4}$$

Vector $\bar{x}$ represents the variables vector, also called *Decision Variables*; its size should be adequate for a complete and simple description of the problem.
f_j are the *Objective Functions*, which are the goals to minimize, depending on the former variables.
The Problem is also subjected to constraints, expressed by *Constraints Functions,* as g_l inequality expression or h_k equality expression. These constraints bound and reduce the solution range, delimiting the decision space in *Feasible* and *Infeasible* regions, as shown in Fig.3.1.

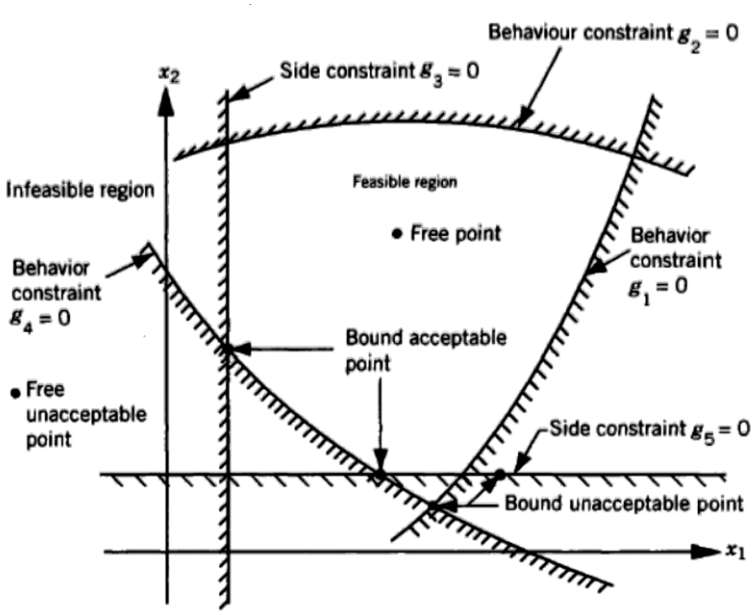

Figure 3.1 *Solution range and possible Constraints.*

In literature, there are different methods to solve MOOP: from *Descend Methods* as Fletcher-Reeves and Newton's proposal, with a differentiable objective function, to *Direct Search Methods*, like Simplex or Grid, that do not require derivatives information. Each method has its pros and cons, for examples the former are able to find the optimum rapidly, but they can stick in local minima.

Hereafter there is a brief description of an optimization approach, as displayed in Fig.3.2. The scheme is composed by two main blocks: Optimization Algorithm and Calculation Model. It will be analyzed in details in Chapter 4.

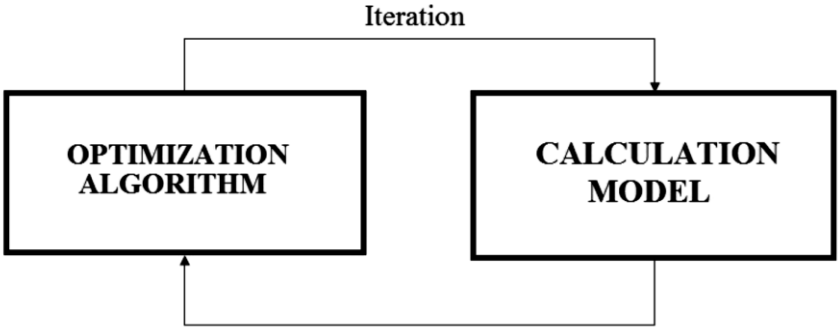

Figure 3.2 *Scheme of an Optimization Problem.*

The first is the mathematical method chosen for solving the problem. The input are the objective functions, depending on the variable vector, and the method calculates a new set of variables that are used by the model to re-evaluate the goals.

Whereas, taking in input the variables, the second allows to calculate the objective functions values. The model can be either a simple expression or a complex series of mathematical equations, such as CFD for fluid dynamics analysis or Patran for finite element methods. The blocks constitute a loop and its iterations go on till a definite convergence criterion or a maximum iteration number.

3.2 Solutions of a MOOP

It is easy to minimize a single objective function and rank its solutions: set $\bar{x}_a$ is better than set $\bar{x}_b$ if $f(\bar{x}_a) < f(\bar{x}_b)$; as mentioned, this is not possible in a MOOP. There are conflicting targets that prevent to univocally define for all objectives which the best solution is. It is necessary to introduce two specific concepts: Dominance and Pareto Front.

3.2.1 Concept of Dominance and Pareto Front

Given two solutions, the Dominance is defined as follow:

A solution $\bar{x}_a$ dominates a solution $\bar{x}_b$ if both following statements are verified:

- *The solution $\bar{x}_a$ is not worse than $\bar{x}_b$ in all the j objectives, which means $f(\bar{x}_a) < f(\bar{x}_b)$, for $\forall j = 1, \dots, J$.*
- *The solution $\bar{x}_a$ is strictly better than $\bar{x}_b$ in at least one objective, which means $f(\bar{x}_a) < f(\bar{x}_b)$.*

Therefore, solution $\bar{x}_a$ is the *dominant* or non-dominated and $\bar{x}_b$is the *non-dominant* or dominated solution.

Figure 3.3 should help in explaining this concept. f_1 and f_2 are the objective functions, the first has to be maximized while the second minimized. Comparing, solution 1 is better than solution 2 because it enhances both goals, so solution 1 dominates solution 2. On the other hand, solution 5 dominates solution 1, because at least solution 5 is better than 1 in one objective, that is f_1.

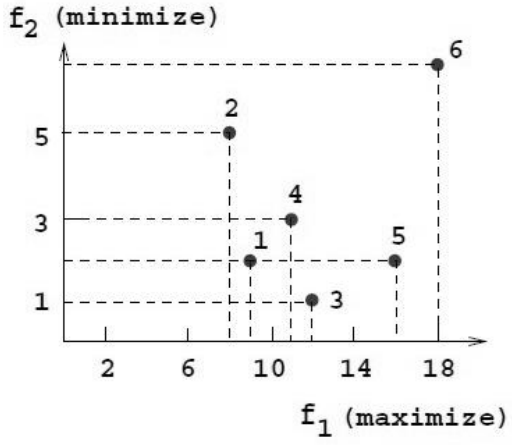

Figure 3.3 *Set of solutions for Dominance concept.*

At the end of all iterations, the *best* possible solutions are the non-dominated; these form and lay on the Pareto Front. Given a dominant set of solution *P,* is impossible to enhance an objective of one of its element without worsening the others.

All Pareto Front solutions are equally optimal for the Problem. In Fig.3.3 the front is composed by solutions 3, 5, and 6.

3.2.2 Advanced Methods

Nowadays, advanced methods like Genetic Algorithms (GA), Simulating Annealing (SA) and Tabu Search (TS) are the best methods to solve a MOOP. They are able to accurately describe and get close to the real front; they give the analyst a proper framework of trade-off solutions, solving more goals at the same time (Fig.3.4). Whereas, classical methods converge slower than the former, mainly because they transform MOOP in single-objective problem, finding only one optimal solution at each iteration.

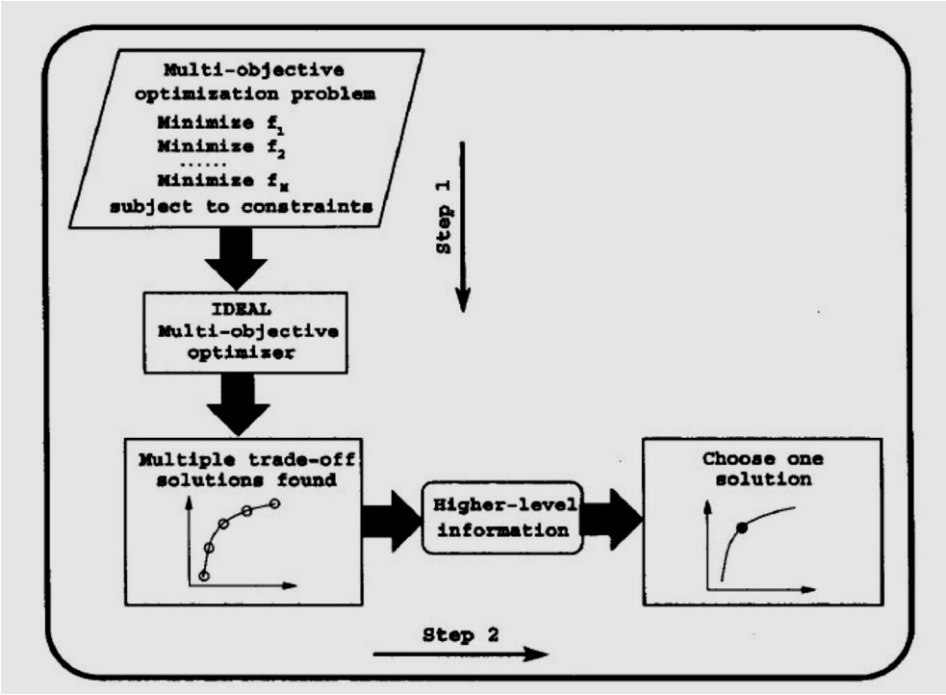

Figure 3.4 *Advanced Process (20).*

Last but not least, engineers have the task and duty to reasonably choose one of the optimal solutions found and complete the design; this choice depends on economical and physical constraints, project requirements or preferences.

3.3 Evolutionary Algorithms

As mentioned, the classical method main problems concern: slow solver convergence, high probability to stick in local minima, low efficiency on parallel machines and dependence on the initial solution.
In the last two decades, *Evolutionary* or *Genetic Algorithms* (EA or GA) have had a key role in efficiently solving MOOPs of different fields, hence they are one of the most used and acknowledged methods.
GAs peculiarity are synthetized in the list below:

- Global algorithms: they hardly stick in local minima.

- Direct methods: GAs evaluate the function in a point, they do not need any information about derivative objectives; they are slower than descent algorithms, but they can be used with all types of functions, even with not differentiable ones.

- Pseudo-stochastic methods: at each iteration, the new solutions set depends both on random and deterministic operations.

- Non-dependence on the starting point: the method do not depend on the random initial solutions. It is able to find the right research directions for minimizing the objectives.

- Parallelization: it is possible to solve the problem quickly on a parallel machine, because GAs work with multiple solutions at the same time.

Obviously, they are based on natural evolution systems; each iteration is called, *generation*, the solutions are named *individuals*, the whole set of solutions is the *population* and the goal functions are named *fitness*. Following the scheme of Fig.3.5, the method starts with a random generation, called Generation 0, then all solutions objectives are calculated and finally a fitness value is assign to each individual. All individuals take part in the creation of the new generation, but as in nature, those with the best fitness values have greater chance to survive during

the evolution. Generation after generation, the algorithms tends to get closer to the real Pareto Front and, theoretically, the last solution should lie on the Front.

A genetic algorithm can act in three different ways to generate a new set of solution, applying Selection, Cross-Over and Mutation operators.

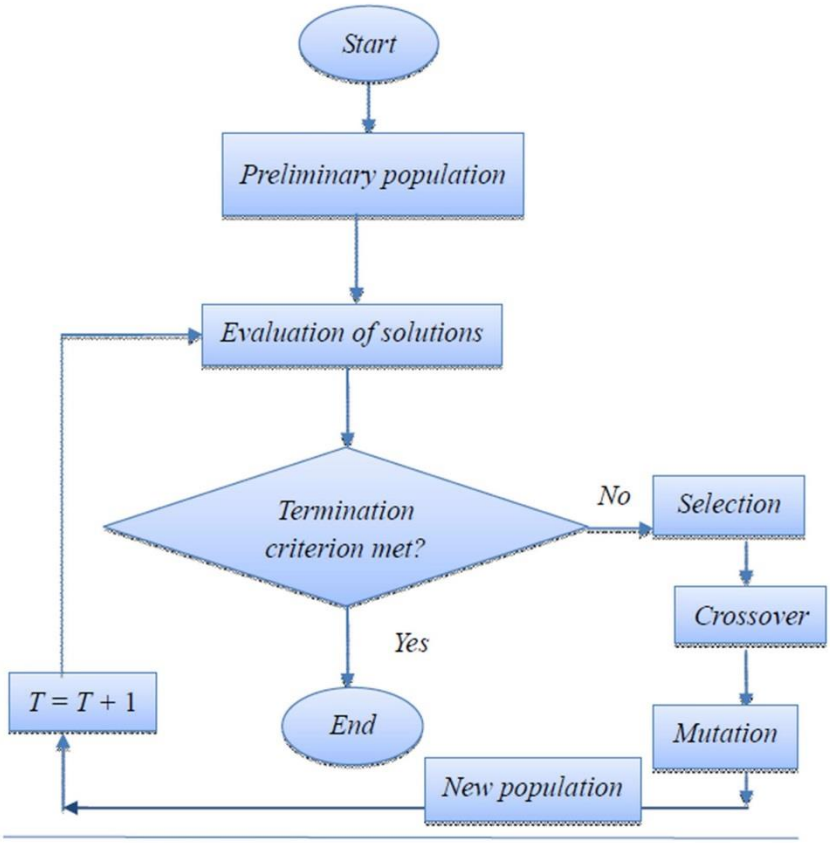

Figure 3.5 *Flowchart of a generic Genetic Algorithm.*

3.3.1 Genetic Operators

Selection. This operator randomly chooses two solutions, the *parents*, which are used by the next operators to generate two new individuals, called *offsprings*. Actually this choice depends on the fitness value assigned to each solution: those with a better fitness have a greater chance to be chosen. In theory, this method allows to create a better generation than the previous one, also maintaining the same size.

There are different types of selection operators, as *proportionate*, *ranking* or *tournament* (21).

Cross-Over. Together with the mutation, the cross-over creates the *offsprings* randomly exchanging part of parents' information; the genetic material is not lost, just recombined. There are different methods for cross-over operation that can be found in literature, like *single-point*, *double-point* or *non-homologous*.

Mutation. This statistical operator maintains the genetic diversity of a generation; for each offspring, a small part of the information is randomly modified. It permits the code to escape from local minima, but it does not guarantee the offspring to be better than its parent.

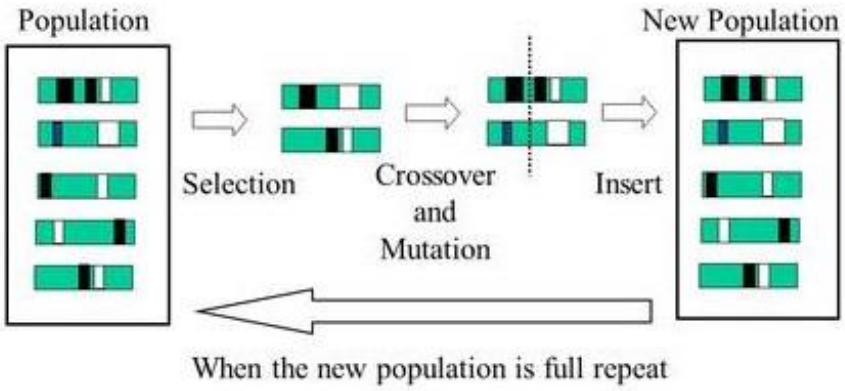

Figure 3.6 *Genetic operators: Selection, Cross-over and Mutation.*

The three operators are shown in Fig. 3.6; they are performed in sequence till a new generation is created that will be evaluated by the calculation model, hence the loop has been closed.

3.4 Non-Dominated Sorting Genetic Algorithm

The mathematical side of this optimization is represented by the Non-Dominated Sorting Genetic Algorithm, developed by Goldberg in 1989 and improved by Deb in 2001 (21). It is one of the most popular and implemented genetic algorithm.

This method works, not only with the already mentioned operators, but also with other three mechanisms: elitarism, preservation of genetic diversity and Pareto ranking.

The NSGA sorts a population *P* on the dominance concept and classifies the individuals in different fronts: all points of a specific front are equally important, as mentioned in Section 3.2.1 and visible in Fig.3.7. A highest fitness value is assigned to the front (front 1) that is closer to the real Pareto Front: the higher is this value, the greater is the probability to survive. That is Pareto ranking.

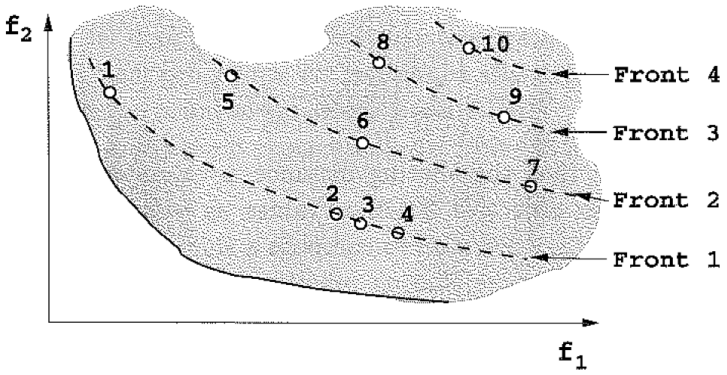

Figure 3.7 *Pareto Ranking.*

Then, to preserve genetic diversity, NSGA assigns a higher value to those individuals which are in less populated area; in this way, it guarantees that isolated solutions have better chance to survive in order to achieve a continuous Pareto front. This step is called *crowding comparison methods* (21).

Finally the last mechanism is *elitarism*: if some solutions are particularly better than the others, these are passed to the next generation without being modified.

The algorithm used in this project is NSGA-II, a variant of the NSGA. It generates an offspring generation Q from the parent generation P and then it sorts the two generations together with the methods mentioned above. Obviously half of the elements must be discarded to go back to the initial generation size. This is shown in Fig.3.8.

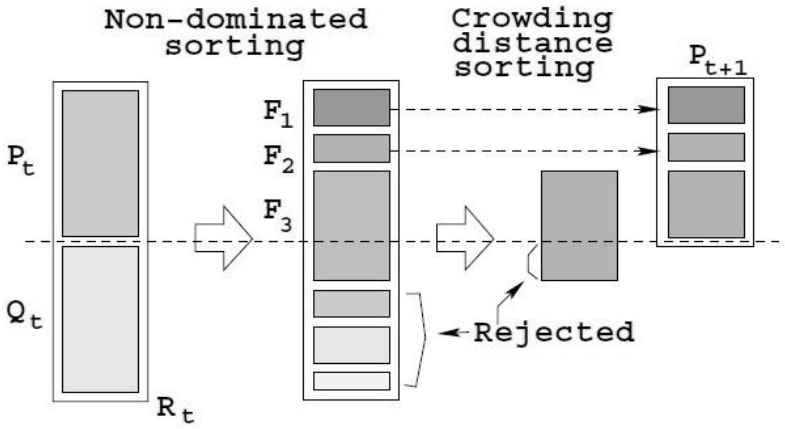

Figure 3.8 *NSGA-II creation of a generation.*

The code has a high computational cost, due to the large amount of calculations required, but thanks to its structure, it is possible to preserve genetic diversity in Pareto Front search.

Summarizing, the NSGA-II of this project has these particular features:

- Selection: *tournament selection*.
- Cross-over: *Simulated Binary Cross-over* (SBX)
- Classical Ranking
- Crowding: for two solutions with the same ranking.

These are described in detail in (7).

3.4.1 Code Validation

This version of NSGA-II has been already tested by Guglielmi on two of the most studied optimization test functions from Deb and Schaffer (21); the test phase is an important step, because it helps to understand what it is expected from the simulations and how efficiently the code performs.

Test 1: SCH1

Firstly, NSGA-II was tested on a single variable problem, with two objective functions to minimize:

$$f_1(x) = x^2 \tag{3.5}$$

$$f_2(x) = (x-2)^2 \tag{3.6}$$

$$-10 \leq x \leq 10 \tag{3.7}$$

In Fig.3.9 are displayed Deb's Pareto Front and Guglielmi's one after 40 generations; clearly, the code works properly providing almost a continuous solution.

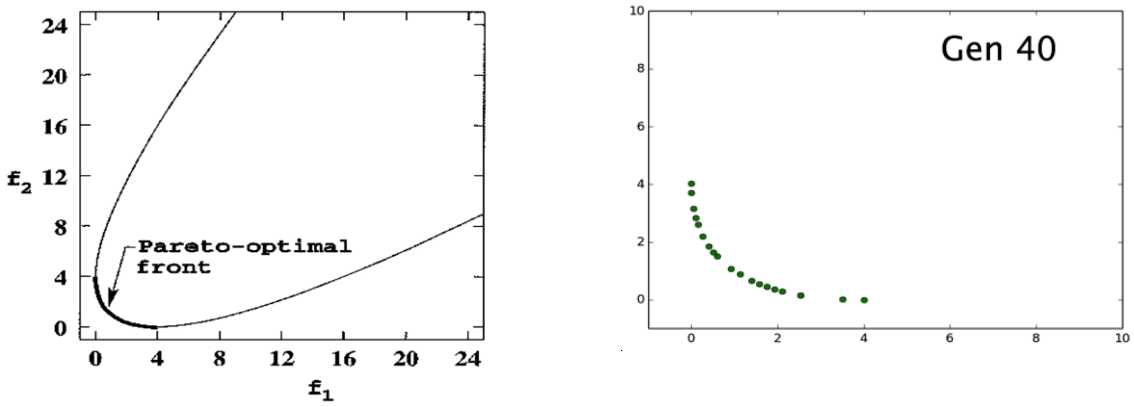

Figure 3.9 *SCH1 Pareto Front of Deb (left) and NSGA-II (right) after 40 generations.*

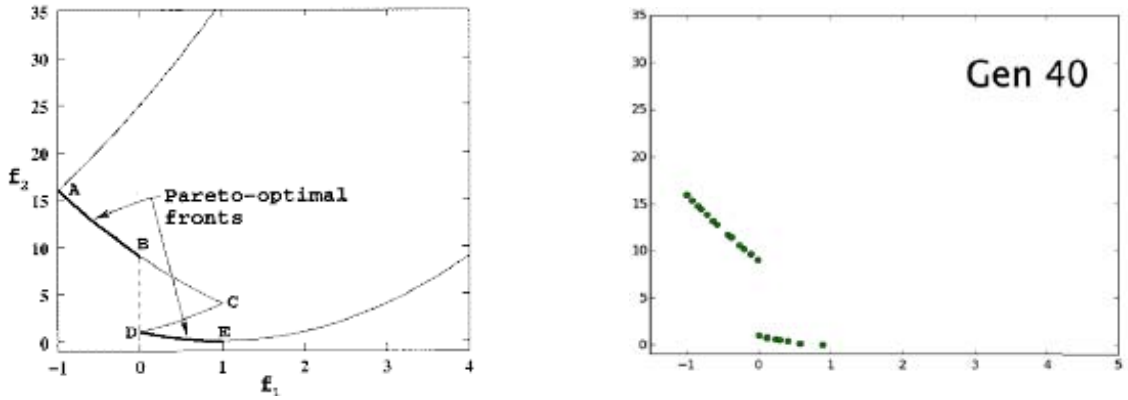

Figure 3.10 *SCH2 Pareto Front of Deb (left) and NSGA-II (right) after 40 generations.*

Test 2: SCH2

Secondly, it was chosen to test the algorithm on a minimizing problem that presents a separate Front:

$$f_1(x) = \begin{cases} -x & x \leq 1 \\ x-2 & 1 < x \leq 3 \\ 4-x & 3 < x \leq 4 \\ x-4 & x > 4 \end{cases} \tag{3.8}$$

$$f_2(x) = (x-5)^2 \tag{3.9}$$

$$-5 \leq x \leq 10 \tag{3.10}$$

Both simulations results are displayed in Fig.3.10; these simple tests prove genetic algorithm capability and its potential in multi-objective optimization problems.

Chapter 4

Methodology

Optimization processes are able to significantly enhance S-duct performances, as mentioned in Chapter 2; in particular, NSGA-II genetic algorithm was applied to a previous project. It provided remarkable results, leading to this further high fidelity analysis.
The objective functions are the Pressure recovery coefficient and the swirl angle at the Aerodynamic Interface Plane (AIP). Both coefficients should be minimize during the simulations, but the algorithm capability is not always predictable because it depends on the specific problem that is investigated.
This Section describes the tools used in the project: the geometry, the optimization methodology, the objective functions and the Fluent solver settings. Guglielmi's research was a really useful starting point for defining a standard approach to the problem.

4.1 Geometry

The geometry used is the one presented by Delot (16) in 2006, designed at ONERA, French Center of Aerospace Research. It is shown in Fig.4.1. As mentioned, this is a scaled up version of Wellborn's duct of 1992 (1).
The centerline is defined by two circular arcs that lie on y-z plane, both with a radius of $R = 665mm$ and a subtended angle of $\theta max/2 = 30°$. The baseline presents an offset and all its cross-sections are circular and perpendicular to the curved centerline.

S-duct centerline is mathematically described by the following equations:

$$x_{cl} = 0 \tag{4.1}$$

$$y_{cl} = \begin{cases} R\sin\theta & 0 \le \theta \le \theta_{max}/2 \\ 2R\sin\left(\dfrac{\theta_{max}}{2}\right) - R\sin\left(\theta_{max} - \theta\right) & \theta_{max}/2 \le \theta \le \theta_{max} \end{cases} \tag{4.2}$$

$$z_{cl} = \begin{cases} R\cos\theta - R & 0 \le \theta \le \theta_{max}/2 \\ 2R\cos\left(\dfrac{\theta_{max}}{2}\right) - R\left(1 + \cos\left(\theta_{max} - \theta\right)\right) & \theta_{max}/2 \le \theta \le \theta_{max} \end{cases} \tag{4.3}$$

In these equations, *R* is the duct curvature, *θ* is the arc angle.

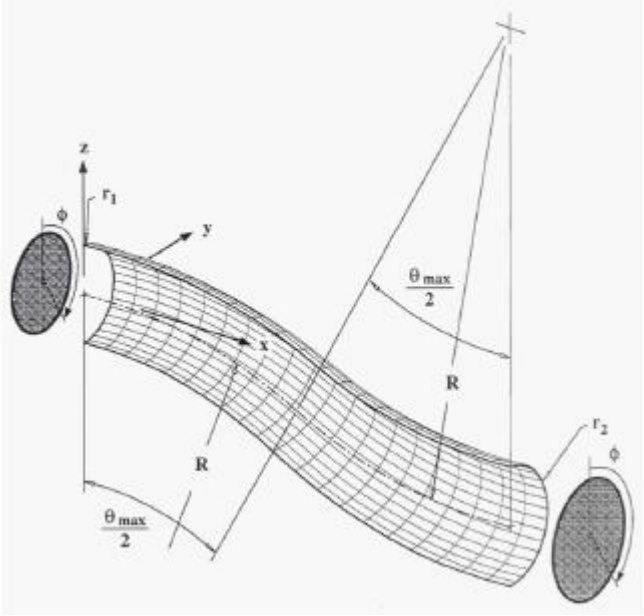

Figure 4.1 *S-duct representation(1).*

The increasing duct radius, instead, is described by the relation below:

$$\frac{r}{r_1} = 1 + 3\left(\frac{r_2}{r_1} - 1\right)\left(\frac{\theta}{\theta_{max}}\right)^2 - 2\left(\frac{r_2}{r_1} - 1\right)\left(\frac{\theta}{\theta_{max}}\right)^3 \tag{4.4}$$

Fig.4.2 is useful for defining the most important geometry parameters.
The inlet has a radius r_1, the outlet has a radius r_2 and a ratio A_2/A_1 of 1.52. The duct presents an upstream straight part of $4xd_1$ and a downstream straight part of $3xd_2$; this is done to ensure uniform inlet conditions and to guarantee that the outlet conditions do not have any influence on the upstream flow.

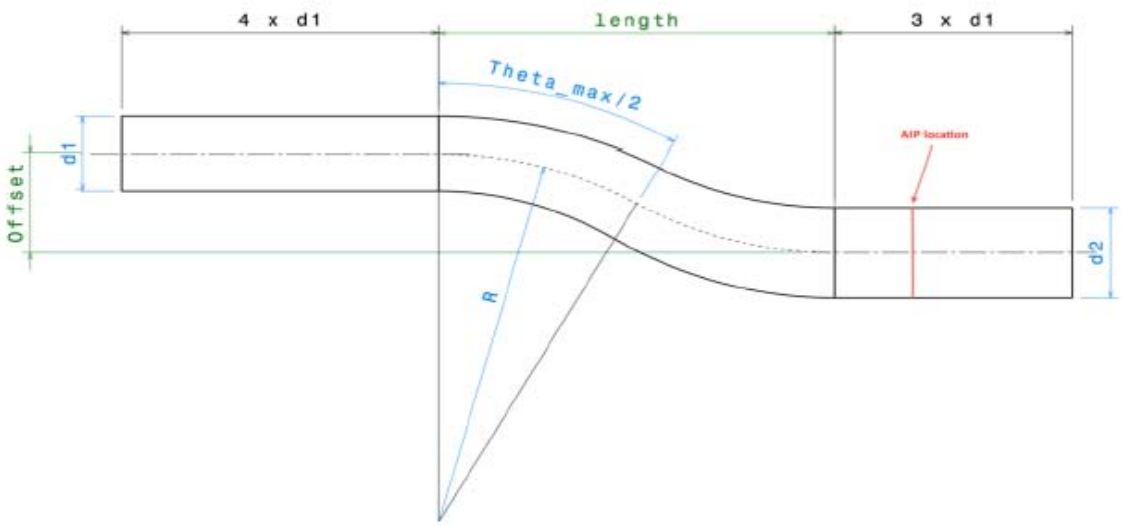

Figure 4.2 *S-duct scheme.*

The geometry parameters are summarized in the two tables below:

Table 4.1 *S-duct geometric parameters.*

Parameter	Value
θmax	60°
R	415.16 mm
r_1	66.5 mm
r_2	82 mm
Offset	324.5 mm
Lenght	658.47 mm

Table 4.2 *S-duct non-dimensional parameters.*

Non-dimensional Parameter	Value
A_2/A_1	1.52
Offset/Length	0.48
R/r_1	6.24
Offset/d_1	2.44

The position of a point inside the duct is specified by the polar angle ϕ, as it is the angle measured from the y axis over a cross section (Fig4.3).

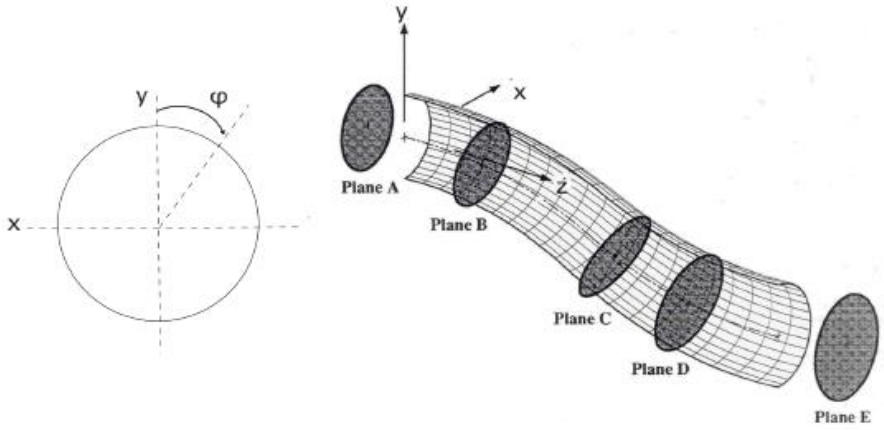

Figure 4.3 *S-duct cross section and ϕ angle (1).*

4.2 Optimization Loop

Chapter 3 introduced the optimization problem and its loop. It consists in two main blocks: the algorithm and the calculation model.

The first takes as input the objective functions, depending on the variable vector, and it gives in output a new set of variables. The second allows to calculate the new objective functions value, taking as input those variables.

The algorithm used is NSGA-II, previously described.

The objective functions are evaluated through a fluid dynamics analysis with CFD Fluent solver (10). Fig.4.4 displayed the classical scheme, also applied in this project (7).

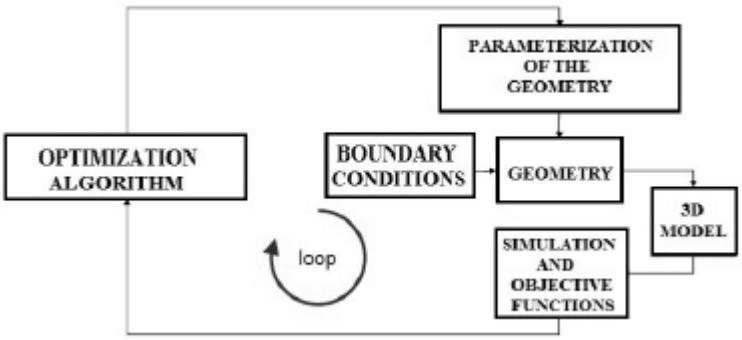

Figure 4.4 *Optimization loop scheme.*

The first step is the parameterization of the geometry, defining variable vector size and control points location. Secondly, the geometry and its mesh are created

in ICEM. Then, the 3D model is imported in Fluent solver, the simulation is set up and run. Finally, the objective functions are evaluated from simulation results, and provided to genetic algorithm, closing the loop.
Great part of the process is automatized, thanks to (7)'s Python scripts. A detail description of the code is in Appendix B.
The right branch of the scheme in Fig.4.4 is described in the following paragraphs.

4.3 Objective functions

As previously described, flowfield behavior in S-duct intakes is very complex and it depends on several factors. One of project aim is to reduce the AIP distortions and make the stream as uniform as possible, improving duct performances by changing its shape.
There are multiplex parameters that can evaluate intake efficiency. Among them, it was decided to base the optimization process on total pressure losses and swirl angle, as in (7) project. Hereafter, there is a brief description of the mathematical expressions used for calculate these goals.

4.3.1 Pressure losses

Total pressure losses are induced by real flow behavior and, especially, by flow separation and vortices, as described in Chapter 2. Pressure Recovery parameter describes these pressure drops. It is calculated with an area-averaged method, later defined for swirl angle (Fig.4.5).
Its mathematical expression is:

$$PR = P_{t,out}/P_{t,in} \tag{4.5}$$

where $P_{t,out}$ is total pressure value at the outlet and $P_{t,in}$ is total pressure value at the inlet.

PR coefficient should be maximized for reducing pressure losses within the duct. The optimization problem is designed to minimize the goals, so the first objective function is defined as:

$$f_0 = 1 - PR \tag{4.6}$$

in fact, minimizing f_0 is equal to minimizing pressure losses, hence maximizing PR value, as desired.

4.3.2 Swirl

The second objective function is swirl angle; the minimization of this parameter allows to decrease flow distortions at the duct outlet, which is also the compressor inlet. As for the former coefficient, swirl is calculated with an area-averaged process, explained through Fig.4.5.

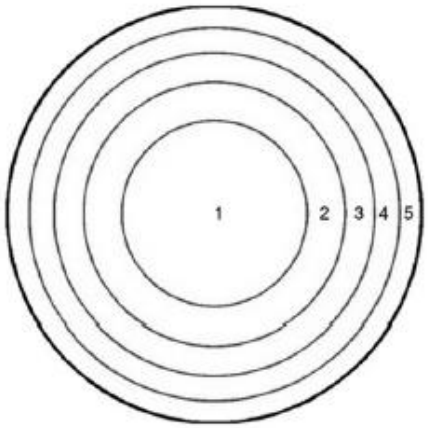

Figure 4.5 *Area-averaged scheme.*

The outlet cross-section is divided into five circle of the same area; then, swirl parameter is calculated for each section and, finally, the five swirl values are averaged, obtaining the final AIP swirl.
Swirl angle is defined with:

$$\propto = arctan(V_\theta / w) \tag{4.7}$$

where V_θ is the radial velocity, defined as:

$$V_\theta = u \sin\theta - v\cos\theta \tag{4.8}$$

where *u*, *v*, and *w* are velocity components along the x, y, and z axis.
So, the second objective function is the area-averaged swirl:

$$f_1 = \propto \tag{4.9}$$

4.4 Parameterization

The first step and one of the most important aspects of an optimization analysis is geometry parameterization. It should be a flexible and simple method, allowing efficient modification of the shape of the S-Duct.
Within this process, the model is described by few geometric parameters (decision variables), not by all its points; this allows to consequently reduce computational costs.
As in (7), Free-Form Deformation (FFD) method is applied. A geometry is surrounded by a rectangular control volume, a proper number of control points is chosen and put externally on the volume. If the control points move, also the geometry will move and will be deformed. The position of each deformed geometry point is described by a weighted sum of the control points position, thanks to Bezier functions. Mathematically:

$$q_{i,j,k}(x,y,z) = \sum_{l,m,n=-3}^{0} P_{i+l,j+m,k+n}\, B_l(x)\, B_m(y)\, B_n(z) \tag{4.10}$$

q is the position of a deformed point, B terms are the B-spline blending function and P coefficients are the specific control points.

4.4.1 Control Points

In this project, the number of control points, and hence the number of variables, was enhanced with respect to (7), (9).
The deformation depends on 80 control points and 36 variables. 2 control points are located in the x direction, 4 on the y direction, and 10 on the z direction, visible in Fig.4.6. For simplicity, only some points are shown in the picture, with the corresponding numeration.

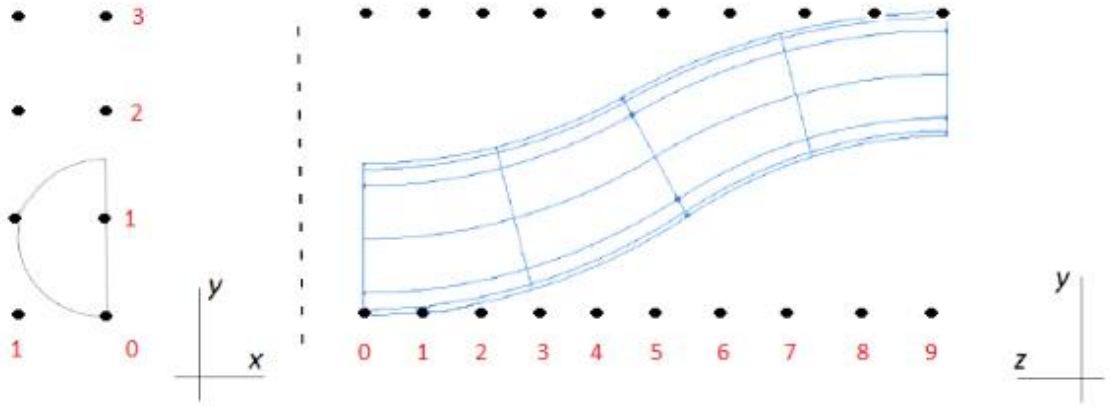

Figure 4.6 *Control Points.*

Theoretically, variables number should be $80x3 = 240$, but thanks to some simplifications and considerations, this number was reduced to 36:

- the points cannot move in the z direction because of manufacturing constraints.
- the points on the symmetry plane cannot move in the x direction, to prevent asymmetric flow.
- 16 points at the inlet and outlet are fixed as a result of manufacturing constraints and the presence of the compressor.
- 16 points between the inlet and outlet cannot move in the y direction in order to guarantee tangential conditions, and to ensure the first derivative's continuity.

Then, it was decided to further limit some of the points, because they are too far from duct surfaces, hence:

- sections 3 and 4: the upper volume may move, the other points are fixed.
- sections 5 and 6: the middle volume may move.

- sections 7 and 8: the lower volume may move.

This new configuration was designed to more intelligently analyze the flow. It is also geometrically more efficient than the previous, because the deformation only considers control points in close proximity to the S-duct surface, and permits to full exploration of the S-Duct's profile with 4 points in the y direction.
This parameterization was used to run two simulations with 50 and 80 mm ranges of variation.

4.4.2 Constraints

In theory, control points variation is not a fixed parameter, but it was put a limit on it for two main reasons.
First of all, optimized geometries can present outer bumps, which interfere with other geometrical constraints. This could especially happen in Distributed Propulsion civil applications, where the engine is embedded in the fuselage.

Secondly, a previous analysis by (7) stated that a variation greater than 80 mm always produce solver divergence or leads to a too high time-cost flow simulation, due to flow complexity.
Between 40 and 80 mm, the solver could diverge from time to time, but it is one of the aims project to investigate new and different geometry configurations, pushing the deformation to its maximum. For these reasons it was chosen
Simulation A is set with a 50 mm variation range, while Simulation B with a 80 mm one, as the most extreme case to analyze. Obviously, solver divergence is expected.

4.5 CFD Overview

4.5.1 Mesh description

After importing duct geometry, mesh-generation step follows. Solving the continuous non-linear fluid-dynamics equations is not possible. So it is necessary

to approximate the domain with nodes (points), connected in a cells network, and the equations are solved algebraically (10).
Mesh or discretization quality influences both time required for solving those equations, that results reliability.
Briefly, there are two types of meshes: *structured* and *unstructured* mesh (Fig.4.7).
The former is defined by a regular connectivity, such as hexahedra in 3D problems. This mesh improved solver convergence because volumes are aligned with streamlines, but is very difficult to build above complex domain.
The latter is defined by an irregular connectivity, easily adaptable on complex geometries. Usually the cells are tetrahedral. The main problem of this mesh is that requires a lot of memory space.

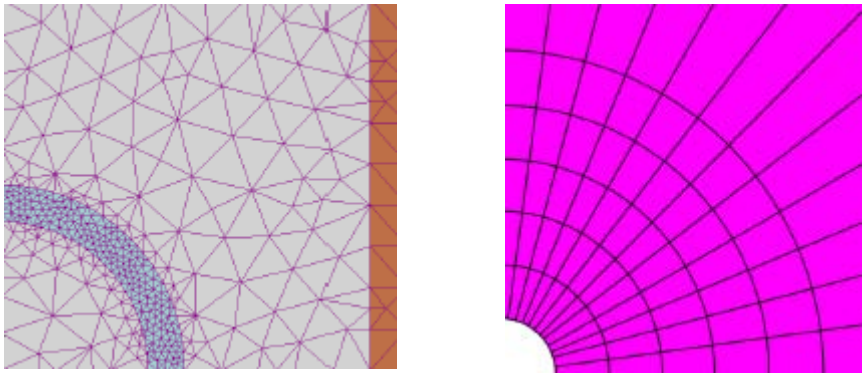

Figure 4.7 *Examples of Unstructured (left) and Structured (right) mesh.*

As mentioned, the work in (7) is able to import *.dat* files for each geometry in ICEM and to build its corresponding mesh with an automated procedure, thanks to Python scripts. ICEM is controlled by a *.rpl* file, containing all the necessary steps. Automatizing the process is fundamental for optimizations problems.

Baseline geometry domain was changed and simplified in order to reduce computing time and speed up the simulations. (Fig.4.8)
Firstly, it was decided to simulate only half geometry, cutting the duct on its symmetry plane. This is possible because the flow is axisymmetric. Moreover that project proved how there are not relevant differences between half or entire duct.

Secondly, the domain was reduced to 2/3 x d_1 upstream and all flow parameters at the distance of 2/3 x d_1 were saved in a *.dat* file, named *InletProfile*. These conditions are used as inlet conditions for the new configuration.

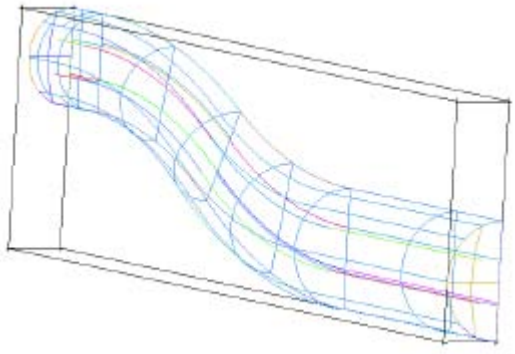

Figure 4.8 *New geometry domain.*

Penin's sensitivity study (22) stated to use an H-O hybrid mesh, as explained in Chapter 2. For Guglielmi's research, it was chosen a medium mesh of 3.2 x 10^6 nodes, later simplified in a mesh of 1.1 x 10^6 nodes. (Fig.4.9)

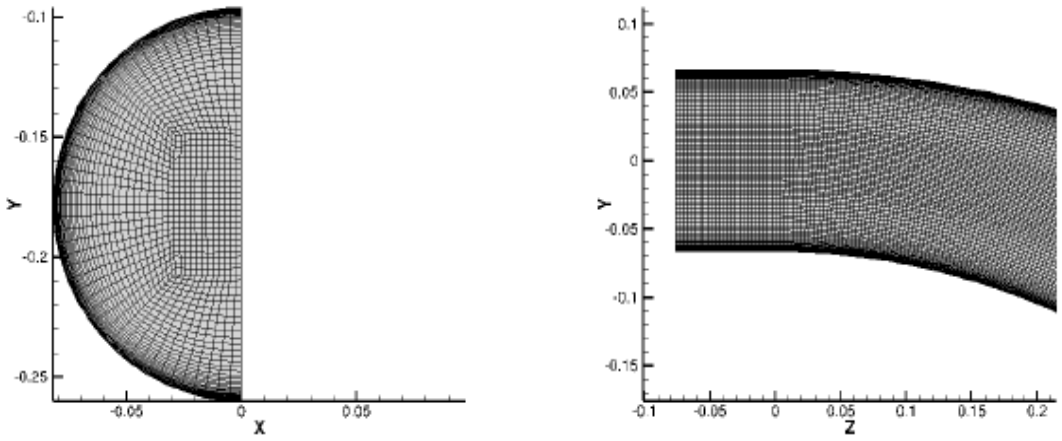

Figure 4.9 *H-O grid at AIP (left), half geometry mesh on symmetry plane (right).*

4.5.2 Fluent Setting Description

The flow was simulated with ANSYS Fluent solver, after importing the mesh created before. All the settings used in this project derive from (7) analysis, because they gave optimal results.
These setting are presented below:

- **CFD model:** RANS model was applied. These equations are commonly used for describing turbolent flows with well-known properties. It solves simplified time-averaged Navier-Stokes equations, achieving considerable results in few time.

- **Air model:** the flow is considered compressible, with an ideal density gas configuration. For describing the viscosity, Sutherland model is applied.

- **Turbulence:** *k-w* SST model is set. For Delot and Penin's considerations, this model is the one that better describe separate region in the duct; it was chosen because one of the objectives is related to pressure losses and boundary layer detachment. Then, compressibility effect, viscous heating and curvature correction were selected with this model.

- **Solver:** Pressure-based solver was set. A flow with an inlet Mach number of 0.6 is considered compressible and the solver suits this inlet condition. The flow was solved coupling momentum and continuity equations, while, for the solution gradients, Green-Gauss Node-based method was used.

- **Initialization**: Full Multi Grid (FMG) was chosen to accelerate solver convergence, initializing the simulations from a good solution.

- **Iterations:** After an iteration sensitivity study, it was chosen to run all simulation for 1500 iterations at second order of accuracy, as a compromise between convergence and time-cost. The residual drops are about 10^{-6} for continuity, velocity, k, energy, omega. Moreover, massflow, Mach number and helicity were check during this phase.

- **Parallel Processors:** The simulations run on Astral, a cluster of parallel processors available at Cranfield University. In theory, one duct simulation takes about 50 minutes on 16 processors.

- **Boundary Conditions:** These derives from Delot's experiments, described in the table below:

Table 4.3 *Boundary Condition for the simulations.*

Boundary Conditions	
Parameter	**Value**
Inlet total Pressure	88.744 Pa
Inlet total Temperature	286.2 K
Inlet static Pressure	69.575 Pa
Outlet static Pressure	78.982 Pa

From the values above, it is possible to calculate the following flow parameters:

Table 4.4 *Flow Parameters.*

Derived Flow Parameters	
Parameter	**Value**
Inlet Mach number	0.6
Massflow	2.43 kg/s
Outlet Mach number	0.37

Chapter 5

Analysis and Discussion of the Results

This Chapter presents and discusses the results obtained throughout this project. The main tasks were flow distortions and pressure losses reductions within the S-duct, thanks to the use of a multi-objective optimization method, combined with the genetic algorithm NSGA-II. The purpose is to produce a flow as uniform as possible at the compressor inlet plane.
The three-dimensional flow was simulated with ANSYS-Fluent solver. The objective functions of the two simulations and the baseline are presented and, when possible, compared between them and with former studies. Then the most interesting Pareto Front ducts are described in detail and related to the ones of a previous project.

5.1 Baseline Analysis

The first and most important step of a numerical simulation is to validate the model used, in order to make consistent the upshots and conclusions achieved. The baseline geometry was simulated, with ANSYS Fluent solver as previously described, and its results were compared with Delot's measurements (16).
Firstly, considering the AIP pressure recovery distribution, Fig.5.1 shows how the model of the thesis is coherent and suitably predicts the experimental data. Besides Delot measured a value of the area-averaged pressure recovery equal to $PR = 0.9711$, while the baseline carried out in this work presents a value of $PR = 0.9691$, with a percentage difference of 0.2%. Therefore it can be assumed

that the pressure trends obtained in the following simulations are reliable and affected by a negligible error.

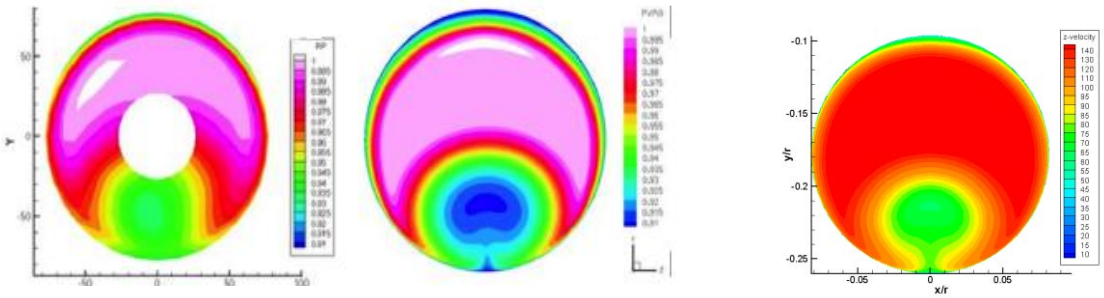

Figure 5. 1 *Baseline PR contours comparison between: Delot experiment (left), Delot simulation (center) and this thesis simulation.*

Secondly, as Delot observed, flow distortion validation is more complicated because of the difficulty in measuring flow parameters; from literature, Penin's research (22) proved how the *k-w* SST turbulence model, the one applied in these simulations, accurately predicts the location of flow separation region and the intensity of the two counter rotating vortices that occur in the duct. Since flow distortion depends on both pressure recovery and flow separation, the model is considered validated and verified.

Table 5.1 includes the objective functions values obtained for the current baseline; these are used as reference parameters for the optimized geometries to evaluate the improvement achieved during the optimization process.

Table 5.1 *Values of the baseline objective functions.*

Baseline Results		
Pressure Recovery PR	$f_0 = 1 - PR$	$f_1 = \alpha\ [deg]$
0.9691	0.03095	3.3978

The following figures prove that the testing baseline is also consistent with Wellborn's experiments and predictions (1).

Fig.5.2 clearly shows flow velocity vectors on the AIP plane, with the two rotating vortices caused by the double bend. It can be also appreciate the symmetrical

flow behavior, because, as predicted, there is no rotation on the symmetry plane ($x/r = 0$).

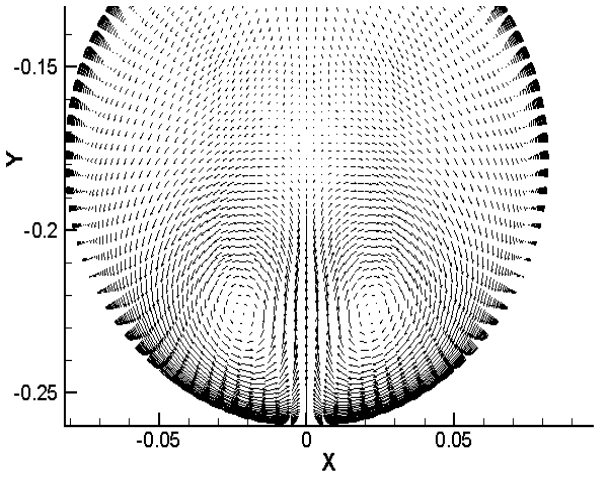

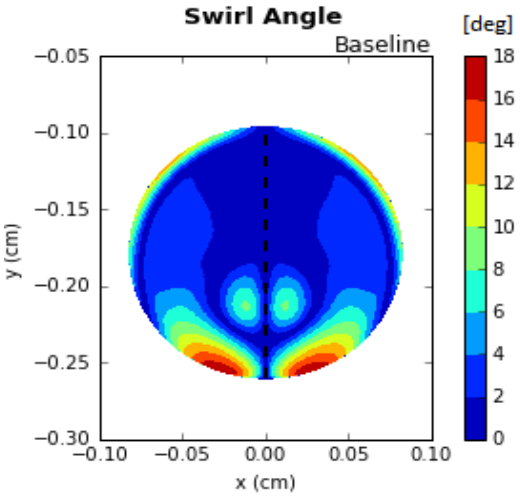

Figure 5.2 *Close-up of velocity vectors at AIP.* ***Figure 5.3*** *Flow distortion contours at AIP.*

Fig.5.3 instead presents the intensity distribution of the swirl *α* for half duct, reminding the simplification applied in the project in Section 4.

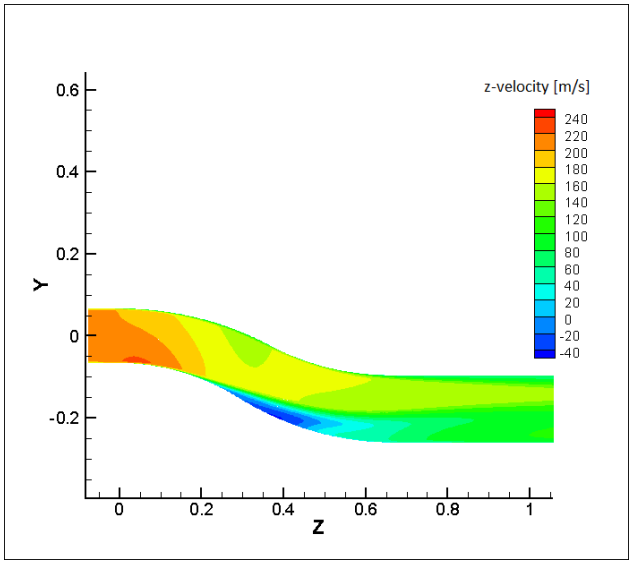

Figure 5.4 *Axial velocity contours on symmetry plane.*

Finally, Fig.5.4 and Fig.5.5 respectively illustrate the axial component of the velocity and static pressure distributions on the symmetry plane; the separate

region is distinctly visible after the first bend and it extends for great part of the duct, while pressure distribution strongly changes along the entire duct.

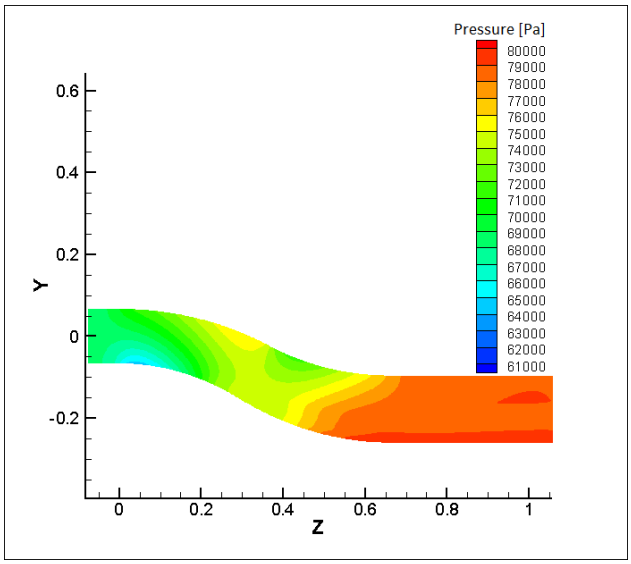

Figure 5.5 *Static pressure distribution on symmetry plane.*

5.2 Results Optimization

The main results achieved throughout the multi-objective optimization method are shown and described in this section. The project carries on Guglielmi's work, modifying and intensifying the way in which the geometry could change.

It is important to remind the readers some settings and parameters used in the analysis. Two simulations, named A and B, were performed with different values of the maximum variation of the control points, respectively 50 mm and 80 mm ($SF = 50$ and $SF = 80$). The design vector is made up by 36 variables, indeed 36 degrees of freedom, on which is based the duct deformation. The size of the generations was reduced from 60 to 40 individuals, mainly due to the time required for 3D geometries testing: the overall process, both considering ANSYS-Fluent and Python elaborations, takes three days for just a single generation of 40 ducts.

Even though the correlation between the number of individuals per simulation and the number of variables used may not seem so adequate, the aerodynamic

improvements and the results achieved are considerate relevant and in agree with those of previous investigations.

5.2.1 Simulation A

Generation 0

As mentioned before in Section 3, the NSGA-II algorithm (coded in Python) randomly creates the first generation, named *Generation 0*, in order to not over constrain the decisional space of the variable vector; this generation constitutes also the starting point for the following ones. Once all the geometries are available, they are run and analyzed with Fluent solver and later post processed. The figure below displays the objective functions of these 40 ducts, compared to the baseline, called Datum.

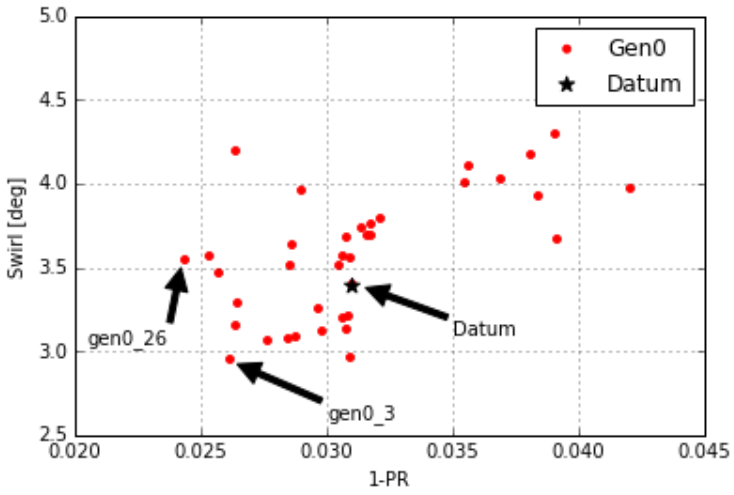

Figure 5.6 *Objective functions values of Generation 0 and the baseline.*

In Fig.5.6 are highlighted two solutions, 0_3 and 0_26, that belong to the very first Pareto Front and are worthy of attention. The former individual presents the best pressure recovery, with a value of $f_0 = 0.0243$, equal to an improvement of 22.44% compared to the Datum; unfortunately, its swirl coefficient ($f_1 = 3.55°$) is higher than the baseline of about 4.47%. On the other hand, both pressure recovery ($f_0 = 0.026$) and swirl ($f_1 = 2.96°$) coefficients for solution 0_3 are better than baseline ones, with a progress of 15.57% and 12.83% respectively.

Even though these geometries have the best PR and swirl angle of the whole Simulation A, they will not be analyzed because this thesis focuses, where possible, on simultaneously enhancing both objective values. Moreover these individuals belong to *Generation 0* that is random and its results do not include the NSGA-II code procedure.

Optimized Generations

The following generations are generated thanks to the genetic algorithm: the optimization process takes as input the objective values of each individual of *Generation 0* to create the new 40 geometries for Generation 1; as before, these are run in Fluent and then post processed to calculate the new objective functions values. These steps were repeated until Generation 8, which is the ninth and last generation analyzed in this work. In total Simulation A tested 360 ducts.

As predicted by Guglielmi, from time to time a $SF > 40$ can lead to solver divergence; this happened in two individuals of the last generation here presented. This fact together with the time required for the simulations, were the main reasons that persuaded to interrupt the optimization process after nine generations.

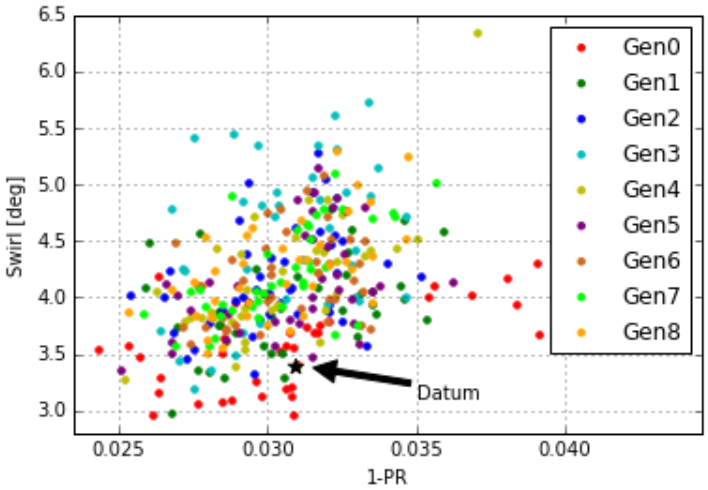

Figure 5.7 *Objective functions values of Simulation A (close-up) and the baseline.*

Fig.5.7 shows a close-up of the whole process progression compared to the baseline.

The picture above may seem not very clear because the point-ducts are extremely overlaid, however the general trend of Simulation A is evident. The algorithm tends to reduce better and more accurately pressure losses than flow distortions. The Pareto Front is composed by few easily identifiable individuals, located in the left-bottom corner of Fig.5.7.

Briefly, Fig.5.8 highlights those ducts and their respective generations that simultaneously belong to the front and better improve both objective functions. These are the geometries, post processed in Section 5.5, with best pressure recovery (5_16), best swirl distortion (1_28) and the trade-off solution (4_32).

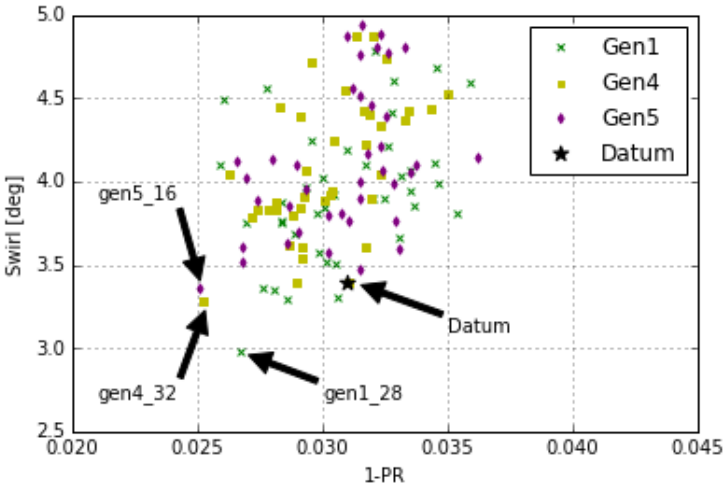

Figure 5.8 *Best generations and ducts of Simulation A.*

Table 5.2 *Comparison between the best geometries and the Datum.*

Optimal Solutions				
Individual	$f_0 = 1 - PR$		$f_1 = \alpha\ [deg]$	
	Value	% improvement	Value	% improvement
Baseline	0.03095	-	3.3978	-
Best PR (5_16)	0.02505	+ 19.03 %	3.3657	+ 0.95 %
Best swirl (1_28)	0.02673	+ 13.61 %	2.9764	+ 12.40 %
Trade-off (4_32)	0.02506	+ 18.56 %	3.2827	+ 3.39 %

In Table 5.2 are summarized the results and the percentage changes of the three ducts compared to the Datum. Again, it is noticeable how the genetic algorithm allows to mainly upgrade the objective functions of about $f_0 = 19.03\%$ and $f_1 = 12.40\ \%$.

To better understand the development and improvements of the optimization method, Fig.5.9 presents all generations in series, excluding the first one. Again here are highlighted the best results of Simulation A and their positions with respect to the Datum.

Equally to Guglielmi's analysis, the last generations (6, 7 and 8) did not upgrade the Pareto Front with new individuals, but the outcomes remained closer to the front, from a general point of view. This trend will be analyzed in details in section 5.3.

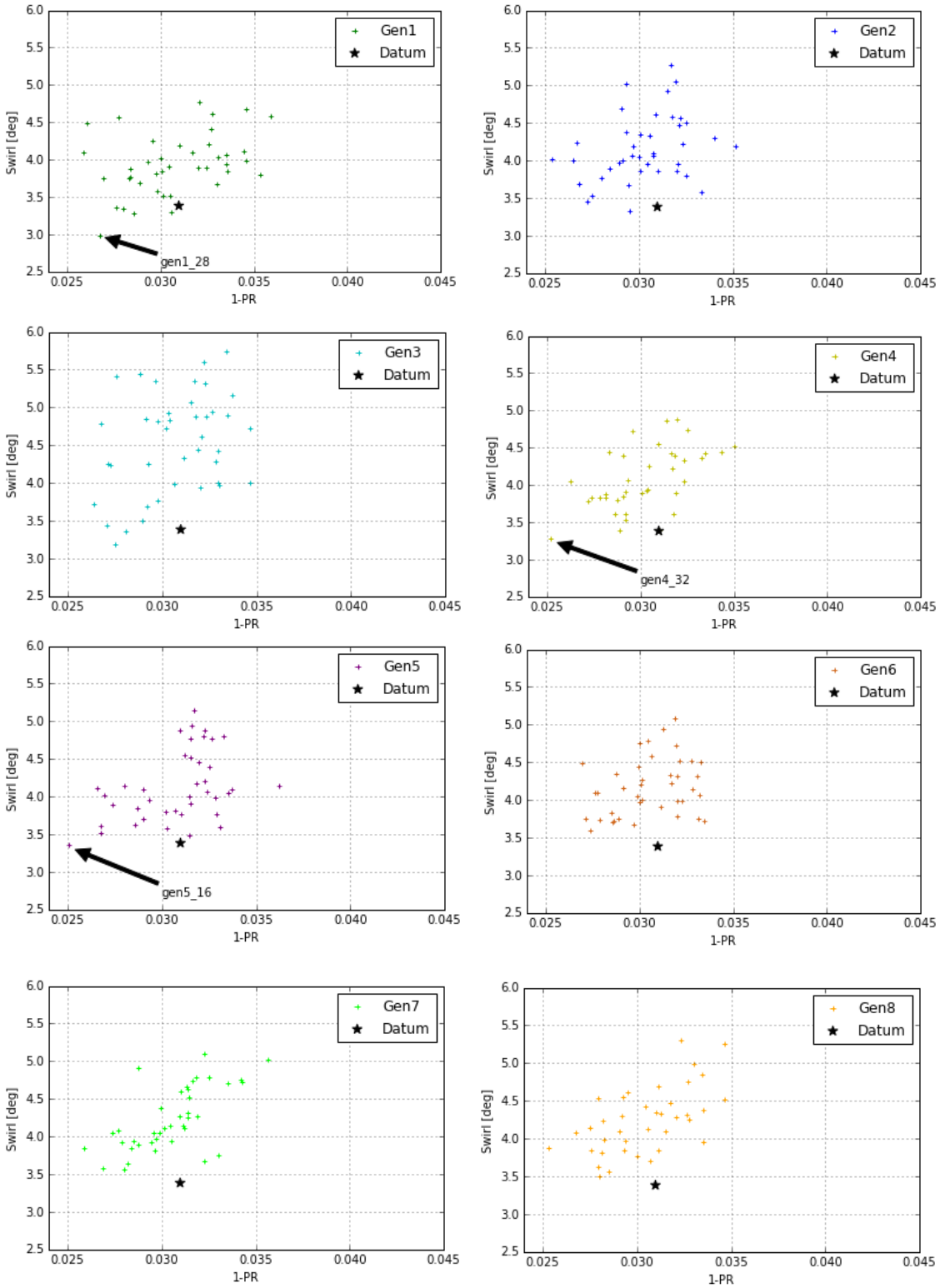

Figure 5.9 *Optimization progression shown generation by generation.*

5.2.2 Simulation B

Generation 0

Following the same scheme of Simulation A, the results of the random generation are hereafter presented and compared with the Datum (Fig.5.10). Initially, due to the greater $SF = 80$ of control points, some geometries of Simulation B show better results than Simulation A. The majority of individuals present a greater improvement in pressure recovery coefficient than swirl angle, as happened for the former system.

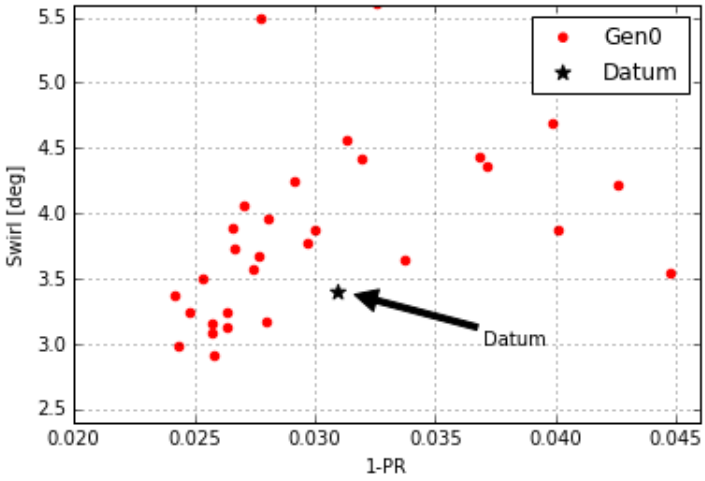

Figure 5.10 *Close-up of Generation 0 in Simulation B.*

Through this configuration it was possible to achieve an enhancement of the objective functions equal to $f_0 = 22.63\%$ and $f_1 = 12.94\%$. It is important to remember that *Generation 0* do not contain the progresses of the genetic algorithm, so for this reason, its individuals cannot be examined.

Optimized Generations

In Fig.5.11 the whole evolution of Simulation B is displayed; it was possible to run the optimization just till Generation 4, so a total of 5 generations and 160 ducts were analyzed. The solver led to flow divergence faster than the previous configuration (A), but it was predictable and expected.

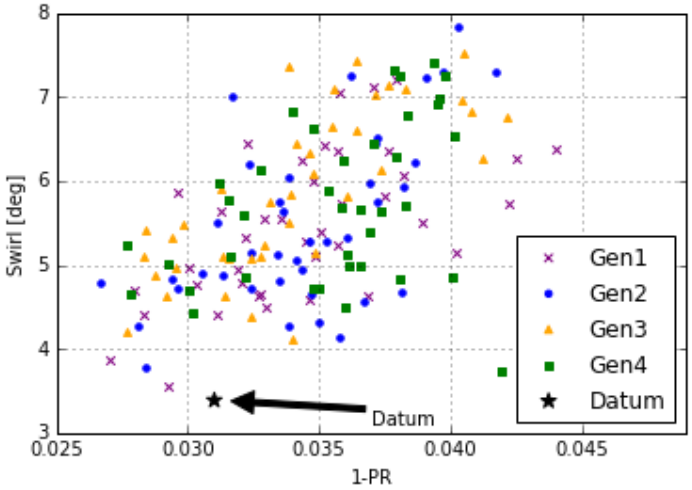

Figure 5.11 *Objective functions values of Simulation B (close-up) and the baseline.*

From the picture above, clearly none of the geometries present an upgrading in swirl angle. Actually, this coefficient tends to worsen, with regard to the Datum, as the algorithm progresses. Nevertheless the code continues to work properly in reducing pressure losses, like it occurred formerly for Simulation A.

Since Simulation B does not improve both goals simultaneously (indeed flow distortion are always higher than the baseline value) and does not reach better results than A, the ducts obtained from this second model will not be considered; only those geometries already mentioned will be examined and compared with the baseline.

5.3 Observations on Simulation A

In section 5.2.1 it was mentioned how overall the results of Simulation A keep getting closer to the Pareto Front and how the code improved more pressure recovery than swirl angle. This trend is noticeable in Fig.5.12 and Fig.5.13 where the mean values of the two objective functions and their standard deviations are displayed along the whole process.

Visibly the mean value of the first goal $1 - PR$ continues to decrease during the optimization, while the second $\propto$ tends to increase (Fig.5.12). It is a further evidence that NSGA-II algorithm works better on reducing pressure losses than flow distortion; this fact depends, not only on the type of optimization method, but

also on the type of physical problem that it is simulating through that algorithm. [Appendix B]

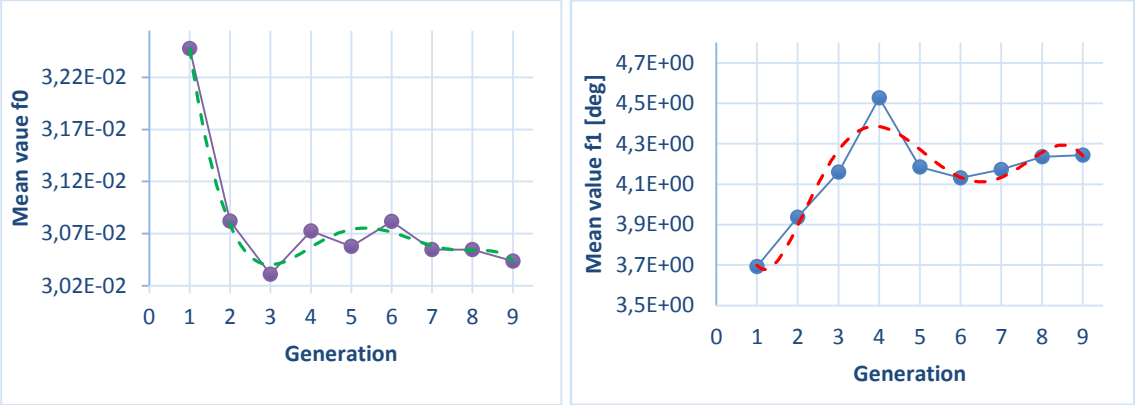

Figure 5.12 *Mean values of objective functions during Simulation A.*

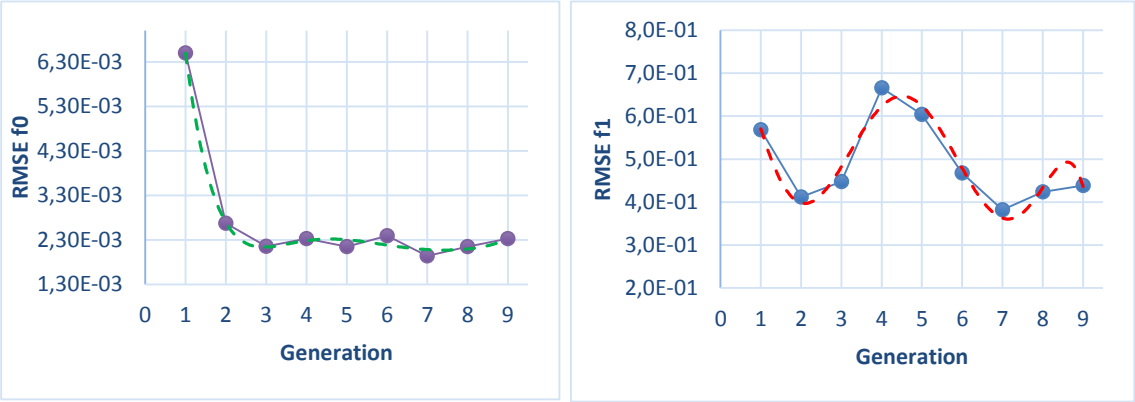

Figure 5.13 *Standard deviations of objective functions during Simulation A.*

Fig.5.13 displays the standard deviations (SD) for both objectives during Simulation A. Standard deviation measures the dispersion of a set of data from its mean; a low SD value indicates that data are getting closer to their mean value. From the graphs, both standard deviations decrease, but it is possible to affirm that pressure losses coefficients deviate less from the mean than swirl angles do, as the magnitude of the former is twice lower.

Both figures point out the general trend of the optimization. Due to the genetic algorithm, all the results tend to get nearest to each other and to be less dispersed, hence it is evident that NSGA-II is moving to the optimal solutions; the

code better recovers pressure recovery coefficient than swirl distortion, as previously described through simulations evolution.

5.4 Comparison with Previous Researches

In this section the chosen ducts belonging to the Pareto Front are compared with Delot experiments and with the results of a former research, carried on by Guglielmi (7). The outcomes are displayed in Fig.5.14 and Table 5.3.
Both projects based the parameterization on Free Form Deformation model (FFD) and the evaluation of objective functions on fluid dynamics simulation, thanks to Fluent solver.

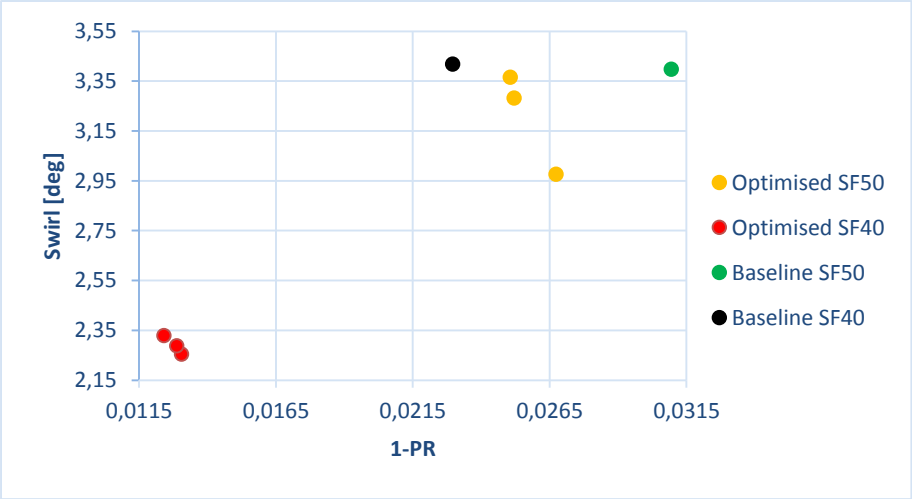

Figure 5.14 *Comparison between Pareto Fronts of a former and the current simulation.*

As it can be seen, the figure above presents the results in term of best PR, best swirl angle and the trade-off solution, with respect to their mutual baselines. The fronts are quite far from each other, so the new model offers the opportunity to investigate and explore different shapes. The outcomes of this project are less performing than Gugliemi's ones; the latter gained a maximum reduction of pressure losses of about 45.97% and of 34.06% for swirl distortion, while the former respectively of 19.03% and 12.40%. Again, the improvement of pressure recovery coefficient is higher than the one of swirl angle.

Despite these data, it can be assert that the simulations run in this thesis are valid and notable. First of all the current work doubled the number of variables, so its results are more reliable and properly describe the flow within the S-duct.
Not always a higher fidelity project brings to better values of the objective functions, but it gets closer to the real phenomenon of the stream.

Table 5.3 *Comparison between the best geometries of current and Guglielmi's simulation.*

Optimal Solutions								
	Current				Guglielmi			
	$f_0 = 1 - PR$		$f_1 = \alpha\,[deg]$		$f_0 = 1 - PR$		$f_1 = \alpha\,[deg]$	
	Value	%	Value	%	Value	%	Value	%
Baseline	0.03095	-	3.3978	-	0.02297	-	3.4185	-
PR	0.02505	+19.03	3.3657	+0.95	0.01241	+45.97	2.3296	+31.85
swirl	0.02673	+13.61	2.9764	+12.40	0.01305	+43.2	2.2542	+34.06
Trade-off	0.02506	+18.56	3.2827	+3.39	0.01287	+43.97	2.2881	+33.07

Secondly, in support of what has just been said, a comparison with Delot's experiments and simulations must be done. Both projects validated the baselines and the model thanks to the tests at ONERA base, which carried out a $PR = 0.9711$; this work differs from that value by 0.21% and Guglielmi's one by 0.61%. Again this fact demonstrates how this model better approximates and describes the real flow, and this is the reason why its results may be considered solid and trustworthy.

5.5 Optimized Geometries

This section focuses on those three geometries that present the best pressure recovery, best swirl angle and the trade-off solution of the project and that are coherent with experimental data. As mentioned, all the S-ducts here post processed belong to Simulation A.

5.5.1 Best Pressure Recovery

It was found how solution 5_16 produces the minimum total pressure losses coefficient, hence the best value of the first objective function f_0.
In Fig.5.15a and Fig.5.15 are respectively displayed its pressure recovery and swirl distortion contours at the AIP plane (left), both compared to the baseline (right).

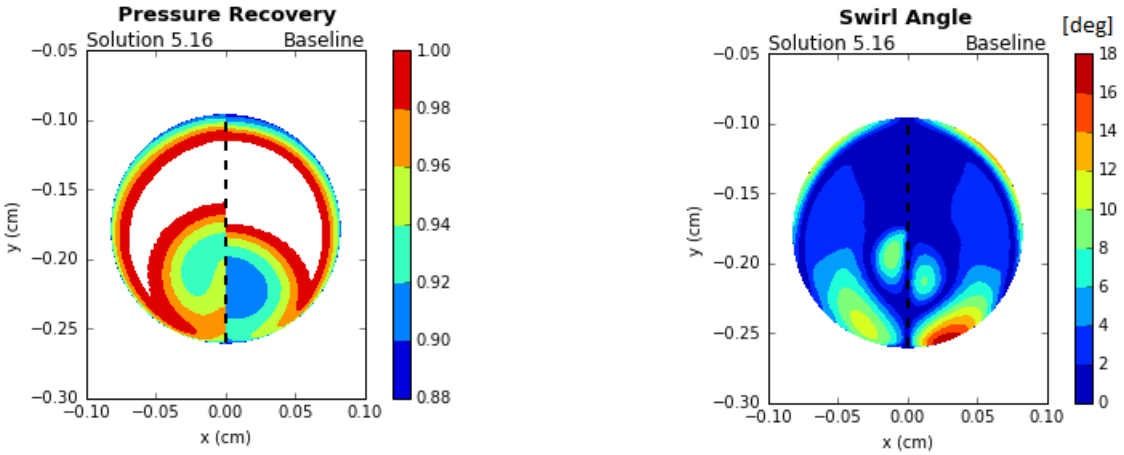

Figure 5.15 *a) Pressure Recovery b) Swirl Distortion of best PR solution and the Datum.*

The geometry gets a percentage improvement of 19.03% on pressure losses, with 1-PR=0.02505 value. The change, clearly visible in Fig.5.15a, is due to the greater uniformity in pressure distributions and to the particular shape of the separate regions, with a wider homogenous bottom-central area. This results at the AIP, which is the duct-outlet, depends on the evolution of the flow within the new inlet silhouette, as shown in Section 5.5.4.
Unfortunately individual 5_16 does not provide such a refinement in flow distortion, in fact $\propto = 3.3657$ with a progress of 0.95% on the baseline value (Fig.5.15b), however it is noticeable a change in its profile contours: vortices are less intense but occupy a wider part of the duct cross-section than in the baseline.

5.5.2 Best Flow Distortion

The best solution, in terms of reduced flow distortion, is individual 1_28. As mention before, it improves the swirl angle of 13.61%, while the pressure recovery

of 15.57%. Distributions of these objective functions at the AIP are shown in Fig.5.16a and Fig.5.16b.

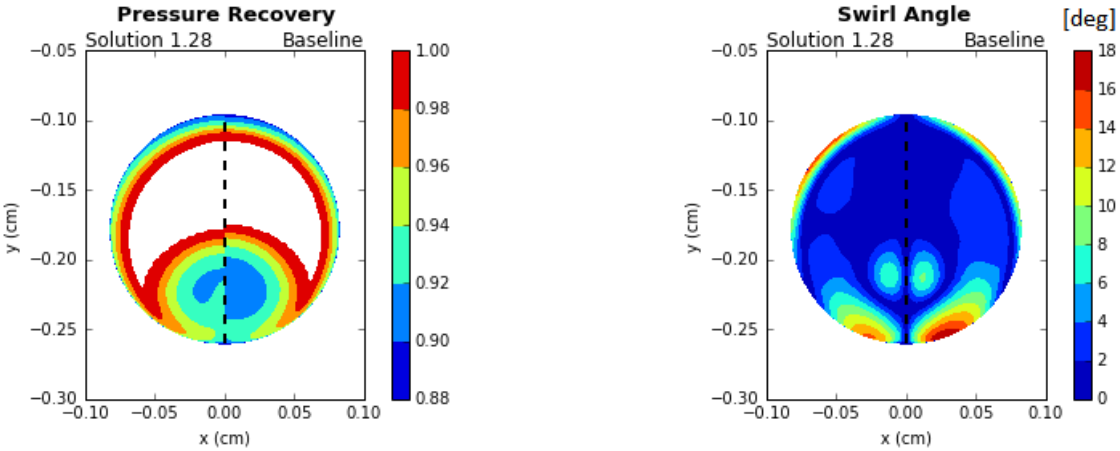

Figure 5.16 *a) Pressure Recovery b) Swirl Distortion of best flow solution and the Datum.*

It is important to remember that the objective functions are calculated through an area-average method. Even if at a first sight, duct 1_28 seems similar to the baseline in PR and swirl shape distributions, but the absolute values of the goals are distinctly reduced. Drawing a comparison also with individual 5_16 and 4_32, it can be seen in the contours size how the current geometry provides a smaller and less intense separate region, as predictable from swirl data.

Again, duct 1_28 points out how the genetic algorithm improves more pressure recovery coefficient than swirl angle and how PR values of the individuals are more alike to each other than those of flow distortion.

5.5.3 Trade-off Solution

Solution 4_32 is the trade-off solution; it is an easy compromise choice between the two ducts analyzed above, because few individuals belong to the Pareto Front and decrease both objectives at the same time.

Below are shown the pressure recovery and swirl distortion contours. As expected from Generation 4 chart, the improvement of f_0 (18.56 %) is higher than the second f_1 (3.39 %) in this individual.

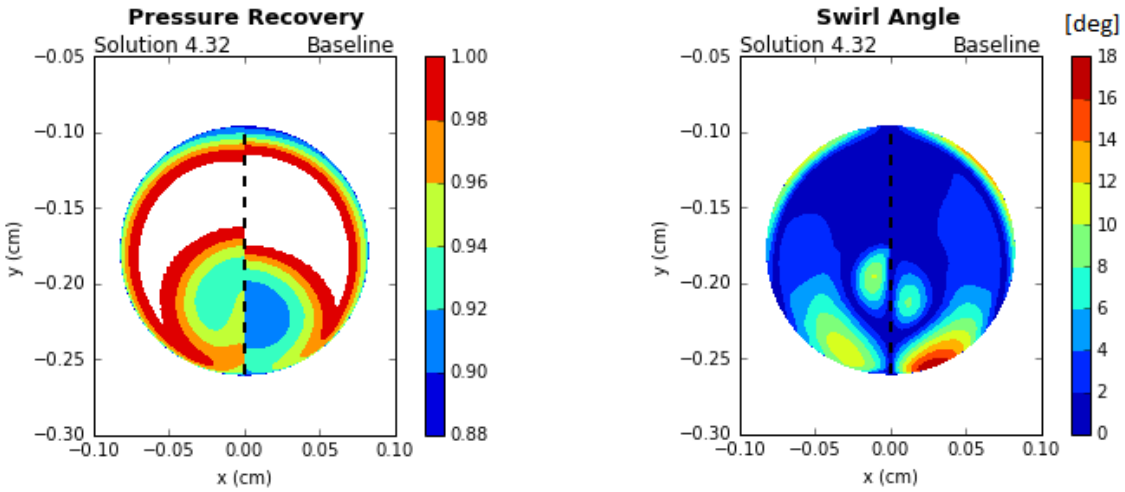

Figure 5.17 *a) Pressure Recovery b) Swirl Distortion of best trade-off solution and the Datum.*

It is also evident from Fig.5.17a and Fig. 5.17b how the AIP profiles are closer to those of solution 5_16 than 0_3. It has a homogeneous separate region at the bottom but a wider separate layer on the walls, while the vortices are less intense but larger than the Datum. The results of this solution are visibly in line with those of the other two individuals.

5.5.4 Symmetry Plane Observations

Hereafter are displayed the symmetry planes of the chosen geometries, their flow axial velocity distributions and static pressure distributions, compared to the baseline. As it can be seen in Fig.5.18, the new ducts present a double curvature on the top and a little bump on the bottom after the second bend. These changes in the duct profile support the reduction of flow distortion and pressure losses.

Total pressure losses are strongly related with the extension of separate region. From the pictures above, all the optimized solutions display a smaller low velocity area than the baseline, in particular the smallest happens in the best PR individual, and a more uniform flow at the outlet; this leads to an improvement of the pressure recovery coefficient, as proved and expected by the simulations.

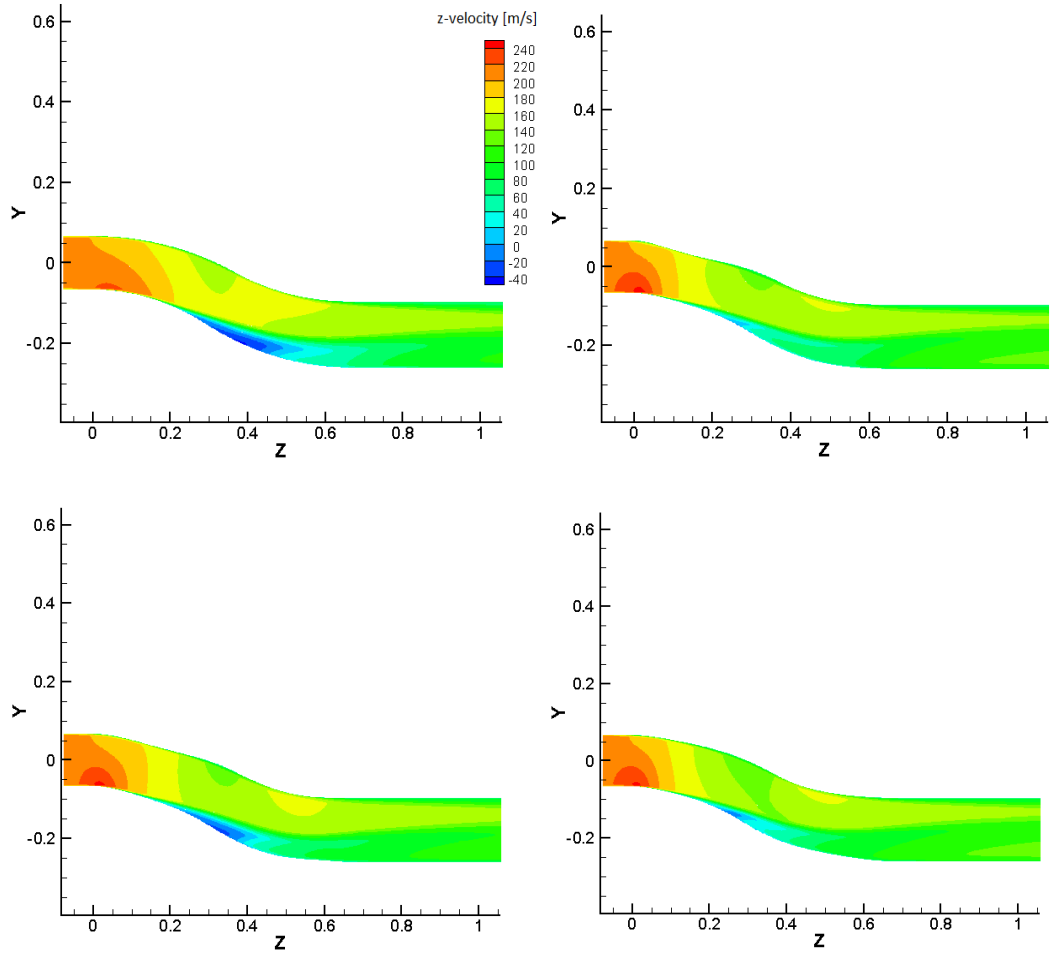

Figure 5.18 *Axial velocity contours on symmetry plane: baseline (top left), best PR (top right), best swirl (bottom left) and trade-off (bottom right).*

Thanks to the new shapes, also the static pressure is more homogenous and higher in the new configurations than in the baseline (Fig.5.19).

The pictures shown below demonstrate how, due to little silhouette modifications, noticeable improvements of the objective functions are achievable. The simulation carried out similar profiles, in which the upper double-bump is slightly unalike than the previous researches, while the bottom bump is coherent. The flow tends to be more uniform in terms of pressure distribution and with a separate region less extended along whole the duct, in particular at the AIP plane as desired.

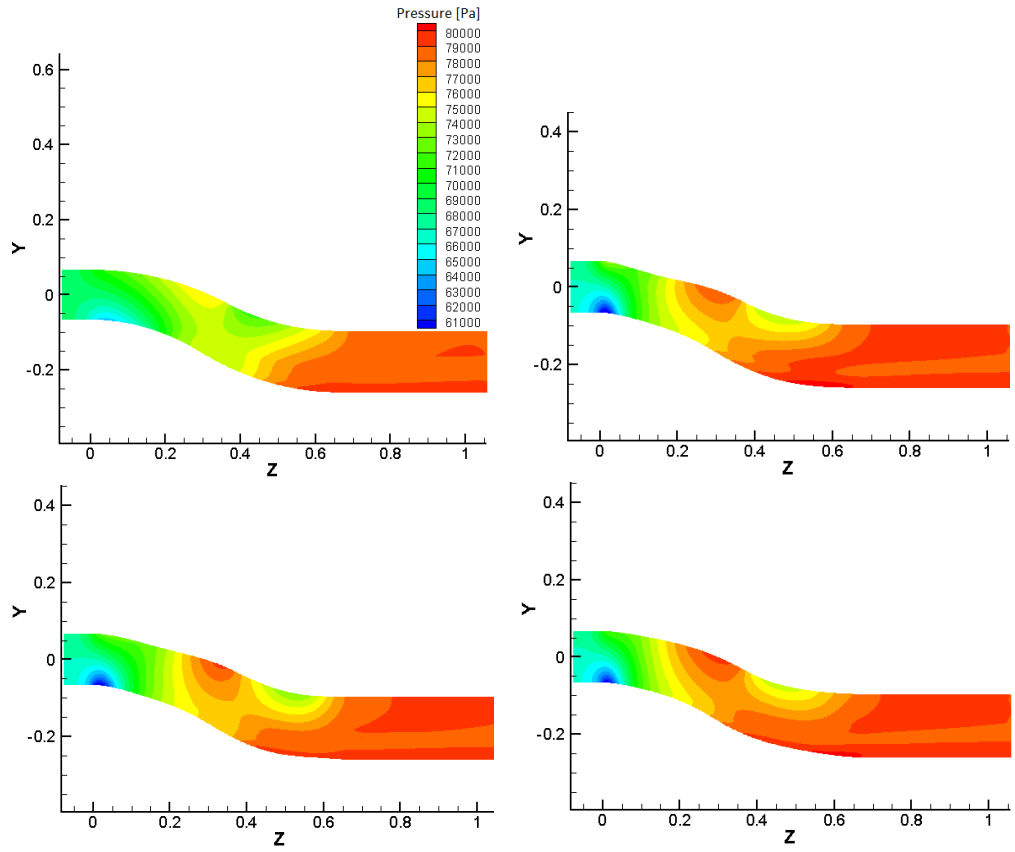

Figure 5.19 *Static pressure contours on symmetry plane: baseline (top left), best PR (top right), best swirl (bottom left) and trade-off (bottom right).*

Chapter 6

Conclusions

The project regarded an S-duct intake shape optimization using the NSGA-II genetic algorithm, to reduce flow distortions and losses at compressor inlet.
The main objectives were to:

- Improve geometry parameterization, increasing the variables number, in order to enhance project fidelity level.
- Bring solver convergence and maximum shape variation to the limit, exploring different possible silhouettes and scenarios.
- To validate and compare the results with a former study.

For the thesis, Delot's S-duct geometry was chosen and parameterized with Free Form Deformation method, using 36 variables. The geometry is deformed in a manner similar to that of former studies: inlet, outlet and also their nearby area were fixed as before, moreover only those volumes and the respective control points around the duct could move. This approach gives more importance to points that are nearest the duct.

Thanks to previous researches, some simplification were made to reduce computational time: only half 3D ducts were analyzed because of flow symmetrical behavior, and the inlet domain was reduced. A coarse H-O mesh of 1.1×10^6 nodes, the k-w SST turbulence model and a RANS methodology were applied on ANSYS Fluent to simulate the flowfield.
The baseline geometry was compared and validated with Delot's experiments.

The optimization process is coded in Python, the same used by Gugliemi and Chiereghin; it is made by several subroutines and scripts that allows to save time, automatizing great part of the loop.
The mathematical side of this optimization is composed by NSGA-II genetic algorithm; Furlan's former studies demonstrated how this algorithm is able to achieve quickly consistent results in aerodynamic optimization problems. The objective functions chosen were swirl angle and pressure recovery coefficient, as, in literature, these are considered the ones that most influence flow uniformity at AIP.

Two simulations were carried out with different variation ranges, respectively 50 and 80 mm; Simulation B stopped due to solver non-convergence, so only Simulation A individuals were noteworthy and showed relevant improvements in both objective functions. After 9 generations and 360 ducts, three geometries with the best pressure recovery coefficient, the best swirl angle and the trade-off were analyzed in detail. The first leads to a decreasing of 19.03% in pressure losses, while the second of 12.40% in swirl distortion, with respect to the baseline.
All the analyzed geometries present a greater enhancement in PR than in swirl angle; probably this is caused either by the code either by physical nature of this problem.

Objectives improvements depend on slight baseline shape variations; as shown before, the geometries present an unalike upper double-bump before the bend and a small bottom bump right after the bend. These shape alterations lead to a substantial reduction of flow separation and pressure losses not only at the outlet, but also in the whole duct

Finally, the results were compared with the ones of a previous project. The outcomes of this thesis are less performing, but more in line with Delot's experiments and simulations. Moreover doubling the variables number, this high fidelity work is more reliable and properly describe the real phenomenon of the flow within the S-duct.

The project showed satisfactorily the changes of a different kind of parameterization, a new geometries examination in an unlike domain region and the improvements achievable in aerodynamic performances of S-duct intakes.

6.1 Recommendations for Future Researches

From the outcomes obtained and the considerations made throughout this project, some suggestions are proposed for further studies.
Firstly, it is recommended to enhance the number of individuals per generation. To run properly the simulations with a genetic algorithm and to improve the results, the quantity of individuals should be adequate to the variable vector size, at least doubled or tripled; this can lead to a better code progression.
As mentioned, the simulations trends were to generate even more geometries closer to the front, but the best results were rapidly achieved thanks to the first generations. Proceeding a greater number of iterations is a further recommendation, in order to add new elements to Pareto Front and to make it more continuous.
Undoubtedly a different and more accurate parameterization should be implemented to describe totally the flowfield behavior and analyze innovative duct shapes.

Then, it is suggested to perform this problem with different optimization algorithms, judging which process is more reliable and valid in the aerodynamic field; actually a colleague is going to execute the same problem with Tabu Search, developed at Cranfield University. Moreover the analysis could present a combination of two different algorithms in the optimization loop: a genetic one to reach easily a proper Front and then a non-genetic one that converges faster to the optimum.

Finally, different objective functions should be processed, fully concluding flow investigations, and experimental tests will be useful in confirming the results of all the projects carried on in the last years.

Appendix A

Inlet Flow Distortions Effects on Compressor Operations

As mentioned in Chapter 2, the flow at the AIP is characterized by strong non-uniformities that negatively affect engine performances and stability; these phenomena reduce compressor operating range and, in the worst cases, can cause surge or stall. There are several types of distortions, but those that are most related to this thesis are swirl and total pressure ones.

A.1 Total pressure

Total pressure distortions mainly depend on boundary layers separation, caused by S-duct shape; the flow presents wide region of low momentum that reduce compressor operating margin. These distortions are divided, according to their dimension and spatial distribution, in radial and circumferential patterns on the cross-sectional area, as displayed in Fig.A.1 (23); pressure non-uniformity always decreases engine stability range, but the most dangerous one is *full-span* distortion, as it causes the maximum loss in compressor stall pressure ratio, when its circumferential extension is $\beta = 60°$, for all shaft speeds, Fig.A.2. For lower β, it is noticeable how the higher is shaft speed, the higher is its influence on stall pressure ratio.

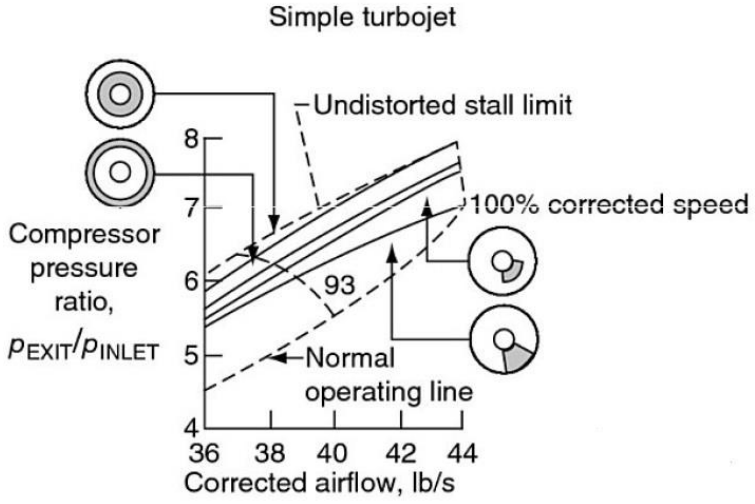

Figure A.1 *Effects of total pressure distortion on compressor stability.*

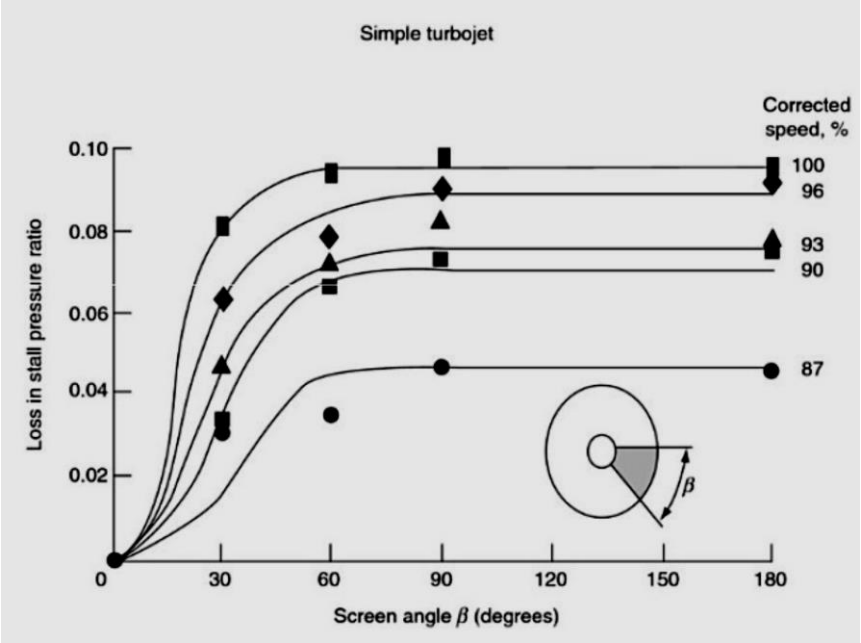

Figure A.2 *Circumferential distortion extension effects on loss in stall pressure ratio.*

A.2 Swirl

Swirls could affect the compressor in different ways, for example:

I. Cross-flow swirl leads to a non-axisymmetric fan loading, especially in Vertical Take-Off and Landing (VTOL) applications. The advancing blades, which rotate in the same relative flow direction, are subjected to a counter-rotating swirl, while the retreating blades to a co-rotating swirl. Hence the blades presents different loads that could cause vibrations and structural damages, compromising the whole engine. In Fig.A.3, it is shown how the engine Equilibrium Running Line is split in two for this situation.

II. Swirl in general implies a deflection of velocity vector from the axial direction; if this deflection is sufficiently wide, it will lead to compressor blades stall. The stall is a phenomenon that occurs when boundary layer separates from blade airfoil profile (either from suction or pressure side), due to large positive and negative angles of attack and substantial total pressure losses arise.

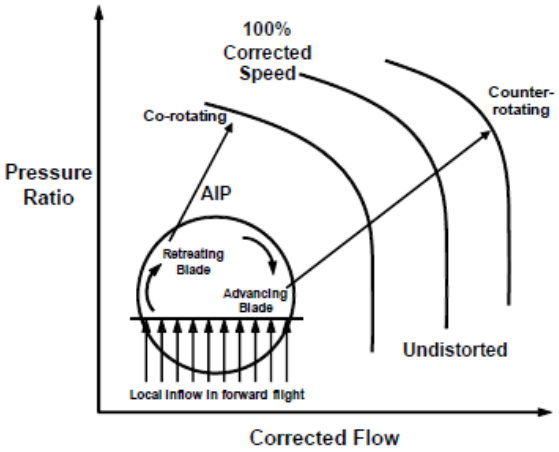

Figure A.3 *Fan Characteristic at constant RPM.*

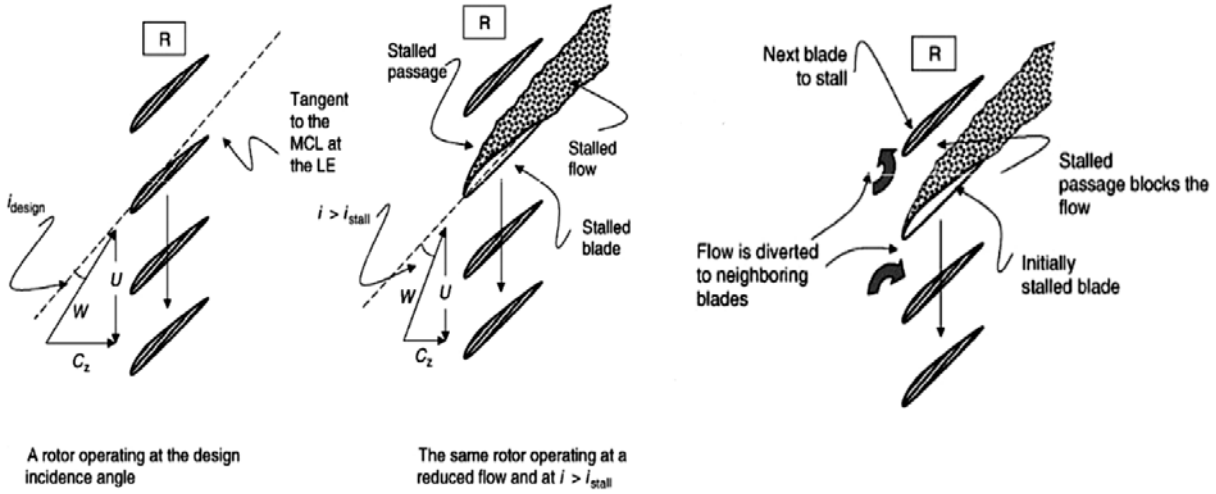

Figure A.4 *Rotating stall scheme.*

As shown in Fig.A.4, if the incident angle of relative flow is greater than i stall angle, the stall appends limiting mass flow through the blades. The stream is split up between the adjacent passages, increasing flow incident angle at the blade above and leading also the latter towards stall; indeed the blade below experiences a reduction of the incident angle and it is pushed away from stall condition. This phenomenon is known as *rotating stall* because it propagates from one blade to another. In a relative reference system, the stall is moving in the opposite direction of blades rotation, while in an absolute reference system the stall has the same rotational direction of the rotor, but at half the speed.

Then, rotating stall can propagate itself in *full span stall* flow, increasing total pressure losses.

Stall mechanism is dangerous for engine operations. It is an unsteady event that causes blades vibration and drives them into resonance, mechanically stressing machine structure; additionally, all non-uniformities make the formation of stalling cells more common, consequently reducing fan efficiency, operative margin and durability, as formerly said for total pressure distortions.

Appendix B

Optimization Scheme

The algorithm applied and the main settings were described in Chapter 3 and 4. Fig.B.1 shows the overall optimization loop scheme, with Python scripts for NSGA-II, geometry and mesh generation, calculation model on Fluent and post processing. Great part of this loop is automated, except for the objective functions evaluation. Hereafter are presented the most important steps.

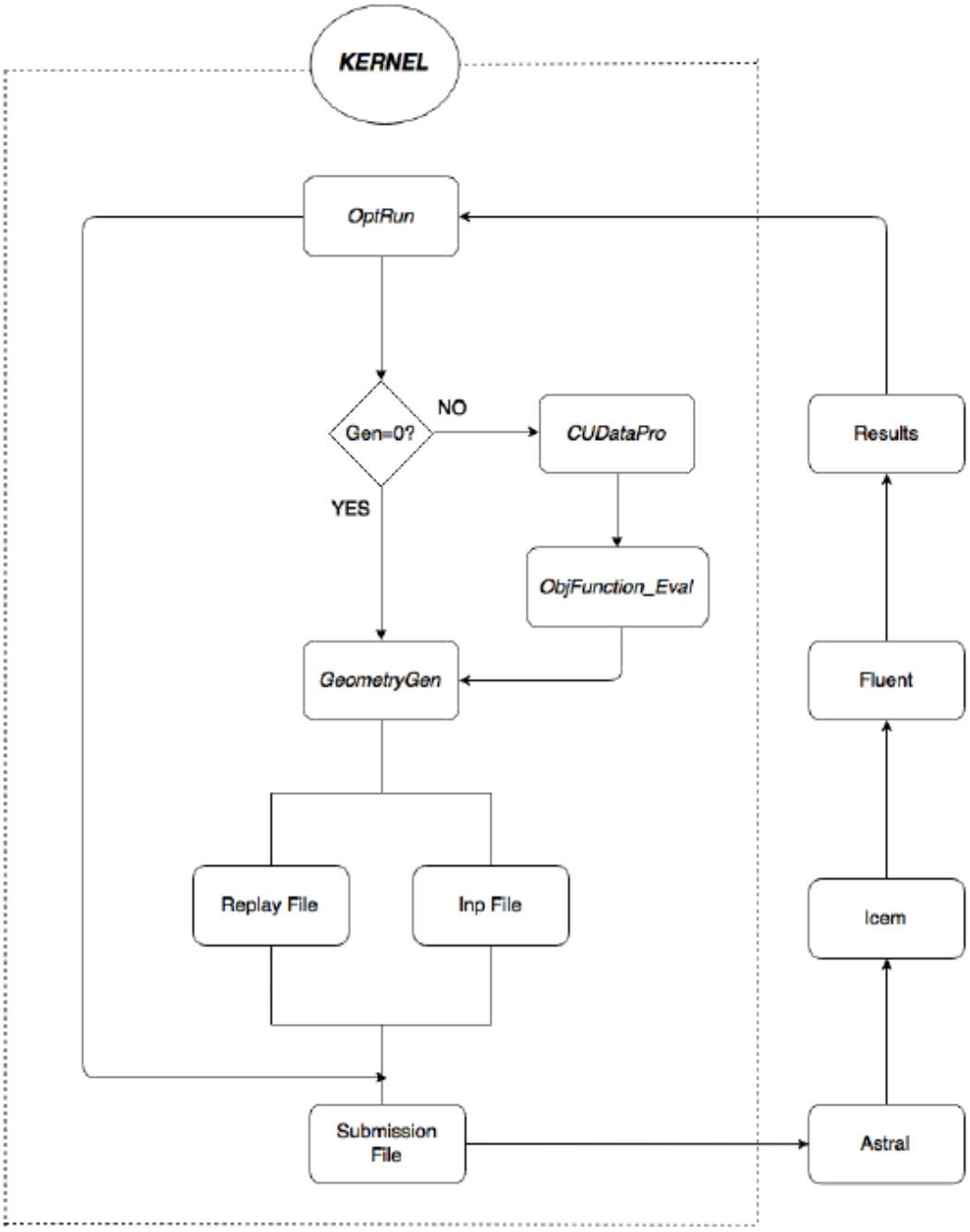

Figure B.1 *Optimization scheme (7).*

- **Optrun:** This script is the starting point of the optimization and controls the entire loop. All numerical parameters are specified: number of individuals per generation, variables vector size, number of objective function and number of constraints. It also runs *OptKernel* and *Fobjective* (in *ObjFunction_Eval*) scripts.
  At the end of each generation, it updates a file *.h5* that stores all the useful data, from decision variables, to individuals and to goal functions.

- **(Opt)Kernel:** Here it is implemented the NSGA-II code, taking the objective function as input and providing the parameters for the next generation as output. It contains several subroutines for *selection, cross-over, mutation* and *crowding*.
  Only once, there is a check in the number of the current iteration: if it is so, it switch to *GeometryGen.*

- **GeometryGen:** This subroutine is made up by several Python scripts and produces the geometries, as *.dat* files, from the variable vector. For each individual, it creates a *.rpl* file and an *.inp* file, respectively containing commands for ICEM and Fluent, in order to easily generate the domain and process the flow, as mentioned in Chapter 4.
  A script, called *WriteAstral*, produces a *.sub* file used in the next step to control Astral.

- **Astral:** The 3D S-duct simulations are run thanks to Astral cluster; it is controlled by a submission file *.sub* where there is a list of instructions: firstly, it creates each geometry and its mesh with *.rpl* file in ICEM, then it sets up Fluent solver with *.inp* file and finally it runs the simulations. Unfortunately, it is required to manually copy *.dat .sub .rpl .inp* files in an Astral directory for every iteration.
  Astral gives in output the essential results (*AIP/sym/wall.dat*) for goals evaluating. This is the most time-expensive step, as it takes about three days to process 40 ducts.
  The procedure is displayed in Fig.B.2.

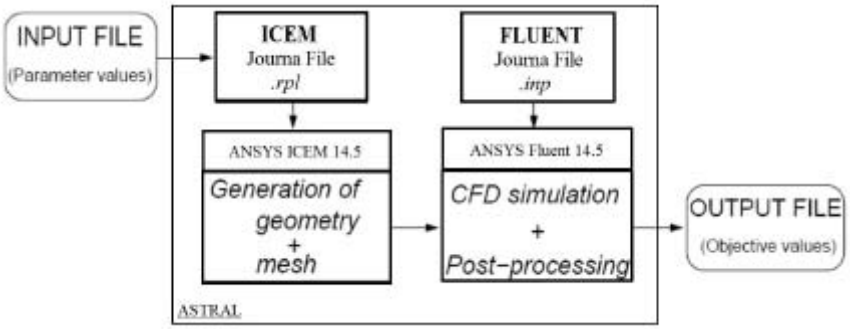

Figure B.2 *Geometry and mesh generation with .rpl and .inp files.*

- **CUDataPro:** Again, it is necessary to manually copy the results on Python directory; this scripts allows to post process the outgoing *.dat* files from Astral and create a set of parameters that describe the flowfield.

- **ObjFunction_Eval:** Taking the parameters above, it calculates the objective functions values of each ducts. Then, it calls *OptKernel* that performs NSGA-II, generating a new variables vector; the latter is passed to *Geometrygen*, which creates new geometries, so the loop has finally been closed.

Bibliography

1. Wellborn S. R., Reichert B. A.*An Experimental Investigation of the Flow in a Diffusing S-Duct.* Nashville, Tennesee : NASA, 1992, 28th Joint Propulsion Conference and Exhibit, pp. 1-12.

2. *Distributed Propulsion Vehicles.* D.H, Kim. Cleveland, Ohio, USA : 27th International Congress of the Aeronautical Sciences, 2010.

3. *Tchnology readiness levels. A White Paper.* J., Mankins. s.l. : NASA Office of Space Access and Technology, 1995.

4. *Design of the Blended Wing Body Subsoni Transport.* H., Liebeck R. 1, Huntington Beach, California : Journal of Aircraft, 2004, Vol. 41.

5. Hardin L.W., Tillma G., Sharma Om P. *Aircraft System Study of Boundary Layer Ingesting Propulsion.* AIAA 2012-3993, Atlanta, Georgia : 48th AIAA/ASME/SE/ASEE Joint Propulsion Conference & Exhibit, 2012.

6. Plas A., Sargeant M., Madani V. *Performance of a Boundary Layer Ingesting (BLI) Propulsion System.* AIAA 2007-450, Reno, Nevada : AIAA Aerospace Sciences Meetin and Exhibit, 2007.

7. L., Guglielmi. *Aerodynamic S-duct intake shape multi-objective optimization for distributed propulsion.* Cranfield University : Msc Thesis, 2015.

8. E., Manca. *Unsteady Aerodynamic investigation of the flow within an optimized S-duct intake.* Cranfield University : MSc Thesis, 2016.

9. M., Barison. *Shape optimization of highly convoluted intakes using genetic algorithms and metamodels.* Cranfield University : Msc Thesis, 2016.

10. *ANSYS fluent theory guide.* s.l. : 14th ed, October 2012.

11. A., Gittings. *Astral-2 cluster user guide.* Cranfield University : s.n., 2012.

12. S-16 Turbine Engine Inlet Flow Distortion Committee. *A methodology for assessing inlet swirl distortion.* Society of Automotive Engineers, 2007.

13. Weske P. *Pressure loss in ducts with compound elbows*. NACA Wartime Repot, 1943.

14. Bandson P, *The flow in s-shaped ducts.* Aeronautical Quarterly, volume 23.

15. Reddy Anderson, Kapoor K. *Study on computing separating flows within a diffusing inlet s-duct.* Journal of Propulsion and Power, 1996.

16. Delot A., *A comparison of several CFD codes with experimental data in a diffusing s-duct,* AIAA, 2013.

17. Fiola C, Agarwal R., *Simulation of Secondary and Separated Flow in diffusing S-ducts.* Journal of Propulsion and Power, 31(1):180-191, 2015.

18. MacManus, Chiereghin, Prieto, Zachos, *Complex aero-engine intake ducts and dynamic distortion,* 33rd AIAA Applied Aerodynamics Cnference, Dallas, 2015.

19. Furlan, Chiereghin, Kipouros, Benini, Savill, *Computational design of S-duct intakes for distributed propulsion,* AEAT: an International Journal, 2014.

20. Deb K., Pratap A., *A fast and elitist multiobjective genetic algorithm: NSGA-II,* IEEE Transactions on evolutionary computation, 6(2):192-197, 2002.

21. Deb K, *Multi_objective optimization using evolutionary algorithm,* Wiley, 2nd edition, 2001.

22. Penin L., *Computational analysis of swirl distortion in a diffusing s-duct,* MSc thesis, Cranfield University, 2013.

23. Farokhi S., *Aircraft Propulsion,* Wiley, 2nd edition, 2014.